

ADJOINT-BASED AERODYNAMIC SHAPE OPTIMIZATION OF A
STRAKE-DELTA WING CONFIGURATION

A THESIS SUBMITTED TO
THE GRADUATE SCHOOL OF NATURAL AND APPLIED SCIENCES
OF
MIDDLE EAST TECHNICAL UNIVERSITY

BY

KAAN YUTÜK

IN PARTIAL FULFILLMENT OF THE REQUIREMENTS
FOR
THE DEGREE OF MASTER OF SCIENCE
IN
AEROSPACE ENGINEERING

SEPTEMBER 2021

Approval of the thesis:

**ADJOINT-BASED AERODYNAMIC SHAPE OPTIMIZATION OF A
STRAKE-DELTA WING CONFIGURATION**

submitted by **KAAN YUTÜK** in partial fulfillment of the requirements for the degree of **Master of Science in Aerospace Engineering Department, Middle East Technical University** by,

Prof. Dr. Halil Kalıpçılar
Dean, Graduate School of Natural and Applied Sciences

Prof. Dr. İsmail Hakkı Tuncer
Head of Department, Aerospace Engineering

Prof. Dr. İsmail Hakkı Tuncer
Supervisor, Aerospace Engineering, METU

Examining Committee Members:

Prof. Dr. Yusuf Özyörük
Aerospace Engineering, METU

Prof. Dr. İsmail Hakkı Tuncer
Aerospace Engineering, METU

Prof. Dr. Sinan Eyi
Aerospace Engineering, METU

Prof. Dr. Kürşad Melih Güleren
Flight Training, Istanbul Aydın University

Assist. Prof. Dr. Özgür Uğraş Baran
Mechanical Engineering, METU

Date: 28.09.2021

I hereby declare that all information in this document has been obtained and presented in accordance with academic rules and ethical conduct. I also declare that, as required by these rules and conduct, I have fully cited and referenced all material and results that are not original to this work.

Name, Surname: Kaan Yütük

Signature :

ABSTRACT

ADJOINT-BASED AERODYNAMIC SHAPE OPTIMIZATION OF A STRAKE-DELTA WING CONFIGURATION

Yütük, Kaan

M.S., Department of Aerospace Engineering

Supervisor: Prof. Dr. İsmail Hakkı Tuncer

September 2021, 63 pages

Modern fighter aircraft compulsorily demand high maneuverability capability, which is mainly provided by an improved aerodynamic performance at high angles of attack. This is achieved by mostly employing strakes and canards. In this study, adjoint-based configuration and leading edge shape optimizations of a strake on a double-delta wing configuration are performed. SU^2 is employed for flow and adjoint solutions. SU^2 flow solutions are first verified on solutions for adaptive grids. In the configuration optimization, the sweep angle of the strake is considered as design variable. In the leading edge shape optimization, the free-form deformation box is employed. Remarkably, it is only allowed to modify the leading edge without changing the flat strake surface. Optimization studies are performed for both inviscid and turbulent flows at 10° and 22.5° angles of attack, respectively. It is shown that the sweep angle optimization based on turbulent flow solutions improves the L/D ratio by about 8.4% at 10° angle of attack and 2.7% at 22.5° angle of attack. In addition, the leading edge shape optimization based on turbulent flow solutions improves the L/D ratio by about 4.5% at 10° angle of attack and 3% at 22.5° angle of attack.

Keywords: double delta-wing, strake, aerodynamic shape optimization, SU²

ÖZ

STRAKE-DELTA KANAT KONFIGÜRASYONUN ADJOİNT TABANLI AERODİNAMİK ŞEKİL OPTİMİZASYONU

Yutük, Kaan

Yüksek Lisans, Havacılık ve Uzay Mühendisliği Bölümü

Tez Yöneticisi: Prof. Dr. İsmail Hakkı Tuncer

Eylül 2021 , 63 sayfa

Modern savaş uçakları zorunlu olarak yüksek manevra kabiliyetine sahip olmalıdır, bu da temel olarak yüksek hücum açılarında daha iyi aerodinamik performansa sahip olmaları gerektiği anlamına gelir. Bu tür performanslar, çoğunlukla kanat hücum kenarı uzantıları ve kanardlar vasıtasıyla elde edilir. Bu çalışmada, çift delta kanat konfigürasyonunda bir hücum kenarı uzantısının adjoint tabanlı konfigürasyon ve hücum kenarı şekil optimizasyonları gerçekleştirilmiştir. Akış ve adjoint çözümler için SU^2 kullanılmıştır. SU^2 akış çözümleri, öncelikle çözüme bağlı adaptif ağ yapılarında doğrulanmıştır. Konfigürasyon optimizasyonunda, hücum kenarı uzantısının ok açısı tasarım değişkeni olarak kabul edilir. Hücum kenarı şekil optimizasyonunda, kullanılan serbest biçimli deformasyon kutusunun, delta kanadın yalnızca hücum kenarı şeklini değiştirmesine izin verilmiştir. Bu sayede hücum kenarının iz düşüm geometrisinin değişmesi sağlanmıştır. Optimizasyon çalışmaları, hem viskoz olmayan hem de türbülanslı akışlar için 10° ve 22.5° gerçekleştirilmiştir. Türbülanslı akış çözümlerine dayalı ok açısı optimizasyonunun, L/D oranını 10° hücum açısında yaklaşık %8.4 ve 22.5° açısında %2.7 iyileştirdiği gösterilmiştir. Ek olarak, türbülanslı akış çözümler-

rine dayalı hücum kenarı şekil optimizasyonu, L/D oranını 10° hücum açısında yaklaşık %4.5 ve 22.5° açısında %3 iyileştirmiştir.

Anahtar Kelimeler: çift delta kanat, hücum kenar uzantısı, aerodinamik optimizasyon, SU²

To my family

ACKNOWLEDGMENTS

I would like to thank my advisor Prof. Dr. İsmail H. Tuncer, for the support through the process. I am grateful to him for all of his effort. I also want to thank Alp Tikenogulları for supporting me through the project.

I would like to offer my special thanks to Assoc. Prof. Dr. Özgür Uğraş Baran for his time and guidance in this thesis. His willingness to spare time for my questions improved the thesis.

My special thanks are extended to Tansu Sevine and Dr. Halil Kaya. They made many crucial contributions to the study by helping with the theory and implementation issues.

I owe my deepest gratitude to my close friends Heyecan Utke Koyuncuoğlu and Büşra Aykaç, for their support and encouragement.

I also would like to thank all my colleagues in the Advanced Air Vehicle Concepts Technology Center of Turkish Aerospace.

Lastly, I would like to thank my dear family that I am proud to be a part of.

TABLE OF CONTENTS

ABSTRACT	v
ÖZ	vii
ACKNOWLEDGMENTS	x
TABLE OF CONTENTS	xi
LIST OF TABLES	xiii
LIST OF FIGURES	xiv
LIST OF ABBREVIATIONS	xvii
CHAPTERS	
1 INTRODUCTION	1
1.1 Numerical Studies	5
1.2 Adjoint-based Optimization	7
1.3 Objectives of the Study	9
2 METHODOLOGY	11
2.1 Gradient-based Optimization	12
2.1.1 Adjoint-based Sensitivity Analysis	12
2.1.2 Surface Parametrization	14
2.1.2.1 Free Form Deformation Box	15
2.2 SU ² : Flow Solver	16

2.2.1	Solution of the Discrete Adjoint Equations	20
2.2.2	Boundary Conditions	20
2.2.3	Solver Setup	21
2.3	Grid Generation	22
2.3.1	Solution Adaptive Grids	22
2.4	Optimization Algorithm	22
3	RESULTS AND DISCUSSION	25
3.1	Reference Study	25
3.1.1	Computational Grids	26
3.1.2	Verification of SU ²	28
3.1.2.1	Solution Adaptive Grid Refinement	30
3.2	Design Variables	30
3.3	Aerodynamic Shape Optimization	31
3.3.1	Shape Optimization at $\alpha = 10^\circ$	32
3.3.1.1	Optimization Based on Inviscid Flow Solutions	32
3.3.1.2	Optimization Based on Turbulent Flow Solutions	36
3.3.2	Shape Optimization at $\alpha = 22.5^\circ$	38
3.4	Sweep Angle Optimization	41
3.4.1	Sweep Angle Optimization at $\alpha = 10^\circ$	41
3.4.2	Sweep Angle Optimization at $\alpha = 22.5^\circ$	46
4	CONCLUSIONS	55
	REFERENCES	57

LIST OF TABLES

TABLES

Table 3.1	Mesh Sizes Used in Mesh Independency Study	27
Table 3.2	Mesh Adaptation Levels	30
Table 3.3	Lift Coefficient	53
Table 3.4	Drag Coefficient	53
Table 3.5	Aerodynamic Efficiency	53

LIST OF FIGURES

FIGURES

Figure 2.1	View of the FFD Box Enclosing a Wing Including Control Points	15
Figure 2.2	Optimization Flowchart	23
Figure 3.1	Reference Configuration	26
Figure 3.2	Surface Mesh	27
Figure 3.3	Volume Mesh	27
Figure 3.4	Pressure Coefficient Values on Upper Surface along Span	28
Figure 3.5	Pressure Coefficient Values on Upper Surface along Span	29
Figure 3.6	Variation of Axial Velocity along Wing Vortex Core	29
Figure 3.7	Spanwise Pressure Distribution on Upper Wing Surface	31
Figure 3.8	Design Variables for Leading Edge Shape Optimization	32
Figure 3.9	Design Variables for the Sweep Angle Optimization	33
Figure 3.10	Variation of Objective Function at $\alpha = 10^\circ$	34
Figure 3.11	Strake Configuration along Optimization Steps at $\alpha = 10^\circ$	34
Figure 3.12	Pressure Distribution on Upper Surface at $\alpha = 10^\circ$	35
Figure 3.13	Streamlines along Wing Vortex and Spanwise Pressure Plots at $\alpha = 10^\circ$	35

Figure 3.14	Q-criterion Contours and Spanwise Surface Pressure Distributions at $\alpha = 10^\circ$	36
Figure 3.15	Variation of Objective Function at $\alpha = 10^\circ$	37
Figure 3.16	Strake Configuration along Optimization Steps at $\alpha = 10^\circ$	37
Figure 3.17	Pressure Distribution on Upper Surface at $\alpha = 10^\circ$	39
Figure 3.18	Streamlines along Wing Vortex and Spanwise Pressure Plots at $\alpha = 10^\circ$	39
Figure 3.19	Q-criterion Contours and Spanwise Surface Pressure Distributions at $\alpha = 10^\circ$	40
Figure 3.20	Variation of Axial Velocity along Wing Vortex Core at $\alpha = 10^\circ$.	40
Figure 3.21	Variation of Objective Function at $\alpha = 22.5^\circ$	42
Figure 3.22	Variation of Strake Shape along Optimization Steps at $\alpha = 22.5^\circ$	42
Figure 3.23	Pressure Distribution on Upper Surface at $\alpha = 22.5^\circ$	43
Figure 3.24	Streamlines along Wing Vortex and Spanwise Pressure Plots at $\alpha = 22.5^\circ$	43
Figure 3.25	Q-criterion Contours and Spanwise Surface Pressure Distributions at $\alpha = 22.5^\circ$	44
Figure 3.26	Variation of Axial Velocity along Wing Vortex Core at $\alpha = 22.5^\circ$	44
Figure 3.27	Variation of Objective Function at $\alpha = 10^\circ$	45
Figure 3.28	Strake Configuration along Optimization Steps at $\alpha = 10^\circ$	45
Figure 3.29	Pressure Distribution on Upper Surface at $\alpha = 10^\circ$	47
Figure 3.30	Streamlines along Wing Vortex and Spanwise Pressure Plots at $\alpha = 10^\circ$	47

Figure 3.31	Q-criterion Contours and Spanwise Surface Pressure Distributions at $\alpha = 10^\circ$	48
Figure 3.32	Variation of Axial Velocity along Wing Vortex Core at $\alpha = 10^\circ$.	48
Figure 3.33	Variation of Objective Function at $\alpha = 22.5^\circ$	49
Figure 3.34	Strake Configuration along Optimization Steps at $\alpha = 22.5^\circ$. . .	49
Figure 3.35	Pressure Distribution on Upper Surface at $\alpha = 22.5^\circ$	50
Figure 3.36	Streamlines along Wing Vortex and Spanwise Pressure Plots at $\alpha = 22.5^\circ$	50
Figure 3.37	Q-criterion Contours and Spanwise Surface Pressure Distributions at $\alpha = 22.5^\circ$	51
Figure 3.38	Variation of Axial Velocity along Wing Vortex Core at $\alpha = 22.5^\circ$	51
Figure 3.39	Spanwise Pressure Distribution for Baseline and Optimized Designs at 75% of the Chord	52

LIST OF ABBREVIATIONS

2D	2 Dimensional
3D	3 Dimensional
ADL	Aerospace Design Laboratory
α	Angle of Attack
C_D	Lift Coefficient
C_L	Drag Coefficient
CFD	Computational Fluid Dynamics
FFD	Free-Form Deformation
FVM	Finite Volume Method
GMRES	Generalized Minimal Residual Method
L/D	Lift-to-Drag Ratio
LEX	Leading Edge Extension
M	Mach Number
HARV	High Alpha Research Vehicle
PDE	Partial Differential Equation
RANS	Reynolds Averaged Navier-Stokes
Re	Reynolds Number
SA-DES	Spalart-Allmaras Detached Eddy Simulation
SU ²	Stanford University Unstructured

CHAPTER 1

INTRODUCTION

Enhanced maneuverability requirements of modern fighter aircraft are commonly achieved with a strake-delta or a double-delta wing configuration [1]. Wing strakes are aerodynamic surfaces attached to the wing leading edge at the wing root. This additional aerodynamic surface may also refer in the literature as "glove", "apex", or "LEX". This device is referred to as strake through this thesis.

In the well-known design book of Raymer [2], strakes are described as being similar to dorsal fins used on vertical stabilizer. Similar to dorsal fins, strakes increase lift for fighter aircraft as high angle of attack maneuver. In addition, strakes provide a stable vortex system. They also delay stall and flow separations on the wing. However, Raymer indicated that application of strakes may result in pitch-up tendencies and performance losses. NASA and General Dynamics tested various strake designs, sizes, and planform shapes [3]. As a result of various tests on strake, a successful strake integration is achieved on an F-18 fighter aircraft by opposing a separated flow with a stable vortex system.

The strake-delta wing configuration originates from the highly swept wing notion, which dates back to the early 1930s. The first successful delta wing application was accomplished by Alexander Lippisch in 1931 [4]. After the demonstration of the potentials of delta wings, the effects of leading-edge vortices on the flow field above the wing attracted more attention. The effects of leading-edge vortices initially are clarified by Polhamus [5–7]. Smith [8] presents a leading-edge suction analogy to solve the flow field for the swept wing, which predicts vortices after sharp leading-edge of the delta wing at low speeds. Lamar [9] improved the leading-edge suction analogy further to predict the effect of side edge vortices of low aspect-ratio platforms.

They also provide a new study and predict vortex flow characteristics for subsonic and supersonic regimes [10]. Rehbach improves the leading-edge suction analogy from solutions of side edge planform to cambered delta wings [11].

As a result of investigations on leading-edge vortices, Küchemann and Lamar [12,13] propose a new wing configuration that incorporates both a common swept wing and an additional aerodynamic surface in front of the wing, which has a highly swept angle and a sharp leading edge to improve the design of swept wings by providing vortex lift to delay the stall. Liu et al. [14] conducted an extensive experimental study. They have categorized the flow patterns observed at the strake-delta wing application and at low speeds with the increasing angle of attack and they have distinguished for different patterns. They have reported that, in the strake-delta wing application, one of the following flow patterns are observed.

- Attached Flow
- Coexistence of Strake Vortex and Attached Flow
- Coexistence of Strake Vortex and Bubble Vortex
- Strake Vortex Breakdown

Stuart [15] provides the development of aerodynamic design of F-5E, evolving from T-38 original wing planform. The original planform did not include a strake at the wing root. A strake of an area ratio of 4.4% of the wing added for F5E. This new development provided a 38% increment in $C_{L_{max}}$ and increased the maximum trimmed angle of attack that is one of the driving parameters of the combat aircraft.

A broad array of lift control devices is evaluated in Lamar's study [16]. The lift control device provides control on vortical flow over the upper wing to enhance lift. These devices are categorized as movable and fixed, where the fixed devices include strakes. Lamar [17] assessed that the planform effect is significant. Chung's study [18] presents that even a strake may have favorable interaction in one strake-wing combination, it may not produce a favorable interaction within another strake-wing combination. Indeed, the necessity of optimizations is indicated in Chung's study [18].

Strake configurations have been studied extensively since the 1970s to find suitable parameters. Luckring [19], in 1979, investigates $\Delta C_{L_{max}}$ changes under the interference effects depending on strake span and wing sweep angle variations. Peake and Tobak [20] address the issue of obtaining the well-organized vortex motions, which can provide significant increasing benefits at the strake-delta wing configuration. Lamar, Peake, and Tobak [20,21] present improvements in maneuverability and a well-behaved vortex system at a high angle of attack with the application of a strake.

Lamar and Fink [22] investigated the best lift increasing with interaction of a strake and wing through a series of strakes. They state that the lift is predicted adequately using an extended suction analogy method, and they found a correlation between the strake span and $C_{L_{max}}$. Also, the lift was enhanced with addition of a strake area. Lamar and Campbell [23] examined leading-edge vortices of strakes, as well as interactions of these vortical flows with neighboring surfaces. Erickson and Gilbert [24] conduct their study on twin-jet fighter aircraft configuration at high angles of attack. They investigate strong potential interactions between forebody and strake vortices. They also point out the formation of a strake vortex varies with the wing spanwise lift distribution. In the study of Rao [25], vortical flow control techniques are studied to deal with the negative effects of leading-edge separation. They investigate vortex interactions on slender body/wing configurations. As mentioned, in the presence of leading-edge vortex, a rapid collapse of leading-edge suction with increasing angle of attack resulted in an inboard movement of leading-edge vortices. Hence, loss of vortex-dominated lift ends in pitch instability [25].

In the article of Polhamus [26] in 1984, the benefits of the implementation of slender wings to modern fighters are discussed. Both variable-sweep and fixed platform wings are presented. For the fixed platform wings, vortex-lift strakes and slender cranked wings are discussed. They expanded the performance by combining the classical attached flow with a strake vortex. This increase in performance is mainly based on improving the design technology with the concept of well-behaved vortex system creation on the upper wing. Bobbitt and Fougner [27] investigated two wing configurations. These configurations are swept wing and cranked delta wing, which is combined with a series of pivotable strakes. It is revealed that the deflection of strakes has a huge impact on moment, on the other hand, it has little effect on L/D .

Rao and Campbell [28] review various vortical flow control techniques including articulated leading edge extensions. Their results show that the planar configuration of strake with wing gives better lift slope behavior than anhedral or dihedral strake configurations. Stinton [29] describes the slender delta wings as two large wingtips integrated at the center line. He represents a slender delta wing with the root strake with a concept with subsonic leading edges and supersonic trailing edges. This concept is useful for delaying stalls at a large angle of attack (more than 40°) because of producing leading-edge vortices by separation at low speeds.

From the aerodynamic perspective, avoiding the flow separation is one of the major wing design considerations [30]. During the design of Concord, attached flow questions are raised up, which affects fighter designs [31]. It is discovered that making the leading edge too sharp induces leading-edge separation. Consequently, sharp leading edge creates a stable vortex system and also gives acceptable low-speed performance.

High Alpha Research Vehicle, HARV, is a modified version of F18. [3] conducted a study to investigate controlled flight at high angle of attack. The vortical flow on the strake is presented in their report including surface and off-surface flow visualizations and extensive pressure distributions at low speeds and angles of attack up to 50° . The results showed that HARV's flow field is affected extremely by the vortex systems, but strake creates a stronger vortex system than the forebody. The strake vortex system dominates the flow field at moderate to high angles of attack until experiencing breakdown with the increasing angle of attack. An extensive survey updating the progress of the investigation on vortex control techniques is presented by Rao [32]. This study involves alleviation of strake vortex-induced twin tail buffet on the F-18. The study remarked that interaction of strake vortices with wing and tail is important. It is the first application of custom-generated large scale vortices to increase maximum lift capacity by integrating highly swept affixed strakes to the leading-edge/fuselage junction.

Brown et al. [33] presents mean and unsteady force and moments from a wind tunnel measurements on a 6% scale model of the F/A-18, including and excluding strake fence. They point out that C_L change is negligible depending the existence of a strake fence. Major ΔC_L is subject to planform and cross-sectional shape of the strake.

In addition to F-5E and F-18 HARV, there are quite a few aircraft with strake in operation, such as F-16, F-22, and F-35.

The main benefits of strake implementation can be summarized as:

- Stabilizes the main vortex, which results in high aerodynamic efficiency [1]
- Low influence on the wing at or below the cruising angle of attack [22]
- Reducing required area for maneuver lift [22]
- Control of aerodynamic center shift [13]

1.1 Numerical Studies

Pioneering numerical studies are conducted by Bloor and Evans [34] in the 80s. They studied the flow field and strake vortex interaction on a strake-delta wing configuration by using the method of vortex discretization, which replaces the shear layer with a distribution of line vortices. It is found that increasing swept angle of a strake resulted in a more stable vortex system creating higher contributions to the overall C_L . The vortex system over the upper wing of a sharp-edged strake-delta wing is investigated by Hsu et al. [35] with a method of solving unsteady incompressible Navier-Stokes equations with a time derivative of pressure added to the continuity equation. Their numerical investigation shows that the first-order-accurate scheme is not adequate to observe the interaction of vortices due to the numerical dissipation.

Fujii and Schiff [36] studied vortical flows on a strake-delta wing by describing the flow field with the thin-layer Navier-Stokes equations. It is shown that the Navier-Stokes equations can present a better solution for the separation and vortex interaction effects on the strake-delta wing. It is also shown in detail how the interaction process takes place at $\alpha = 12^\circ$, and the bubble vortex-breakdown developed at $\alpha = 30^\circ$, while the spiral kind of vortex-breakdown occurs at $\alpha = 35^\circ$, where α represents the angle of attack.

Thin layer Navier-Stokes equations represent the vortex system better, but it is more expensive than Euler equations. Reznick and Flores [37] studied vortical flows around

the F-16A aircraft by solving flow field with a combination of Euler and thin-layer Navier-Stokes equations. According to results of the pressure distribution, numerical results were in agreement with experiments.

Yin [38] investigated the rolling up of leading/trailing edge vortex sheets formation and their interactions for the configuration of delta and strake-delta wings. The numerical results based on a simple two-dimensional discrete vortex model are in conformance with the experimental results [39]. The results show that there are two separate vortices, inboard vortex and outboard vortex, at a low angle of attack. However, they start interacting with each other at a high angle of attack in a strake-delta wing configuration.

Another numerical study, which solves the flow field with the Euler and RANS equations, points out the junction of the strake and wing in a flat strake-delta wing has important effects on the vortex trajectories and breakdown [40]. Consequently, it affects the aerodynamic performance of the wing. The same model in the Verhaagen's et al. experiment [41] is also investigated at $M = 0.22$ by solving the flow field with thin-layer compressible Navier-Stokes equations [42]. Ekaterinaris et al. [42] state that grid resolution around vortex is important at a high angle of attack to represent vortex system. Verhaagen [42] discusses numerical solutions comparing past experimental results and states that they are in good agreement, but it is obvious that viscous effects dominate the boundary layer, and the associated pressure distribution.

In 2007, Sohn and Chung [1] attempted to control the vortical flow upon the wing surface in another well-known model by changing the planform shape of the strake. It is revealed that planform has a large effect on the vortex flow pattern, and hence pressure distribution around the strake-wing combination. The model used in the study of Sohn and Chung [1] was introduced as a reversed strake, and it is compared to the conventional one. It is stated that a higher lift value can be possible at the high angle of attack with the reversed strake configuration [18]. Another parameter that affects the pressure distribution on the upper wing and the vortex initiation is the leading edge shape, and it is found that the leading edge shape creates different lift characteristics, especially at a high angle of attack [43]. For both wing and strake, the oncoming flow collides with the strake leading edge first, causing the flow to separate

at the leading edge. Primary strake vortices are generated when the divided flow rolls up into a pair of counter-rotating vortices [43]. Hence, shape-optimized strakes have different leading-edge formations and form different vortices with associated characteristics in terms of line of action and strength.

Arasawa et al. [44] conducted a numerical study on another model by using a high order scheme. Numerical results predict aerodynamic coefficients properly, and strake-wing vortices are indicated, on the other hand, there is still a discrepancy for the location of vortex merging. A more detailed study on the interaction of vortices originating from the leading edge of strake and wing stated that vortex breakdown location has vital importance in predicting the aerodynamic forces and moments. Another numerical and experimental study for a $65/40^\circ$ strake-delta wing focused on lift coefficient prediction shows that numerical results are in good agreement with experimental results up to the post-stall region [45]. Another work of explaining vortex structure is presented by Zhang et al. [46]. They point out that vortex-breakdown is heavily affected by the distance between strake and wing vortices and how they develop.

A well-known study on the Verhaagen's et al. experiment [41] employs a high fidelity and expensive SA-DES method [47]. The numerical results reported that there is a strong interaction between the strake and wing vortices involved with the development of the cross-flow vortices at 22.5° angle of attack. In addition, the pressure distribution is reasonably in concordance with the experiment also.

1.2 Adjoint-based Optimization

Optimization is the way of seeking the state to give the best result under certain conditions. There are gradient-free and gradient-based methods that are compared in the Lyu's et al. study [48]. In the present study, gradient-based optimization is used, and it is one of the best efficient optimization methods which uses the benefits of direction information. Fundamentally, gradient-based optimization problems consist of objective functions (one or more objective functions can be defined), constraints that are limited to solution set, design variables, and the direction information, which is derivative of the objective function with respect to design variables.

The critical point of a gradient-based optimization problem is calculation of derivative of the objective function. There are different methods for the evaluation of derivatives. The first approach is finite differences based on the perturbation of design variables and solving the flow field for each perturbation. Another one is the direct approach subject to linearization of the governing equation and then evaluating the sensitivity of the entire domain, but the linear solution equations become a dominant cost. However, the adjoint approach is slightly different, and a dual of the linearized problem is constructed for each objective function. The adjoint approach allows easy and cheap calculation of sensitivity information so that derivative of the objective function is for many design variables [49]. Consequently, in aerodynamic problems, the adjoint approach is always beneficial. The adjoint approach is also divided into two techniques, the continuous method in which the governing equation is linearized and adjointed, then they are discretized, and the discrete method in which the system discretized and then performs linearization and adjoining.

The first sensitivity analysis with continuous adjoint in fluid mechanics is prepared by Pironneau [50,51] for the Stokes equations, and then he implemented the methodology for the incompressible Euler equations. In 1988, Jameson [52] introduced the sensitivity analysis procedure for the inviscid compressible flows and conducted optimization of transonic airfoil. The method reached wide usage with the high efficiency based on increasing design variable range [53].

However, the first announcement of the discrete direct method dates back to 1982 by Bristow and Hawk [54] for the panel method. Implementation of the compressible Euler equation is studied by Elbana and Carlson [55]. Despite the direct method studies, Baysal and Eleshaky [56] firstly introduced the adjoint of the discretized equations, and it is followed by Frank et al. [57] for one-dimensional duct flow. Taylor et al. [58] presented their study on sensitivity analysis in turbulent flows. Sensitivity analysis becomes an important method in evaluating gradients [59]. Sensitivity analysis of Navier-Stokes equations on unstructured meshed is finally implemented by Anderson et al. [60].

In aerodynamic shape optimization, the Free Form Deformation (FFD) Box technique is a common geometric method to control simple deformations on rigid bodies. It is

built on the concept of enclosing an object inside a cube or another hull object and altering the thing within the hull when the hull deforms. Alternatively, there is a lattice structure around the baseline geometry. Design variables are defined onto this lattice structure, and they control the deformation by applying displacements to the vertices onto the surface and smoothly interpolated into the field. FFD Box technique is first developed and introduced in study of Sederberg et al. [61] to carry through deformation of solid geometries and adapted for the aerodynamic shapes by Samareh [62]. It is firstly used for an airfoil section in aerodynamic shape optimization as a geometry generator applied in each optimization cycle [63]. The method was successfully introduced in aircraft wing optimization by Brezillon [64] for optimization of DLR F6 aircraft wing geometry. FFD Box method can be simply explained as a tiny structured mesh. Herein, successful researches that use the FFD Box method in aircraft wing optimization are presented by Lyu et al. [65] and Secco et al. [66]. Optimization of design features of a wing such as a sweep and a taper ratio is studied by Leoviriyakit [67]. It is indicated that the planform of the wing can be optimized by using the adjoint method, and gradients depending on design features can be obtained with the projection of sensitivity values. In the literature, there is no such optimization study on strake, which subjects the sweep angle of the stake and the leading-edge shape by using FFD boxes.

1.3 Objectives of the Study

This study aims at performing an adjoint based aerodynamic shape optimization of a strake for a strake- wing configuration. The configuration used in the experimental study of Verhaagen's et al. [41] is taken as the baseline configuration. The leading-edge profile and the sweep angle of the strake are chosen as the design variables, and the L/D ratio is taken as the design objective.

SU² is employed for the flow and the adjoint solutions on solution adaptive grids. The optimization process is driven by DAKOTA. The adjoint based optimizations are performed for both inviscid and viscous flows, and the results are assessed.

The method employed in this study is presented in the next chapter in detail. The

verification and optimization studies, the optimizations based on inviscid and viscous flows are presented in the Results and Discussions chapter. Concluding remarks are stated in the last chapter.

CHAPTER 2

METHODOLOGY

In the present study, the main objective is to develop a shape optimization procedure for a strake to improve the aerodynamic efficiency of the strake-delta wing configuration, C_L/C_D , using a gradient based optimization process. The shape optimization focuses separately on the leading edge profile and the sweep angle of the strake. The gradient vectors along the optimization process (sensitivity derivatives) are obtained by the adjoint solutions of the RANS equations. Open source CFD solver SU² is employed for the solutions of both the RANS and the discrete adjoint equations. The methodology employed in the present study is described in the following subsections:

- Gradient-based Optimization
 - Adjoint-based Sensitivity Analysis
 - Surface Parametrization
- SU²: Turbulent flow and the adjoint Solver
 - Solution of Discrete Adjoint Equations
 - Boundary Conditions
 - Solver Setup
- Grid Generation
 - Hybrid Grids
 - Solution Adaptive Grids
- Optimization Flowchart

2.1 Gradient-based Optimization

The gradient-based optimization is an iterative process to minimize the cost or any objective function (lift, drag, etc.) with respect to pre-defined design variables. This iterative process requires gradients or sensitivity derivatives of the objective function with respect to the design variables. Once the gradient vector is evaluated, a line search process drives the optimization. In this study, the optimization process is driven by the open source software DAKOTA and the Quasi-Newton method available. The quasi-Newton method requires calculating the gradient and the Hessian of flow parameters. The gradient information is provided by the discrete adjoint solver in SU², and the Hessian is numerically evaluated based on the BFGS method.

An optimization process of function $f(x)$ can be defined as;

$$\text{minimize } f(x), \quad x = [x_1, x_2, \dots, x_n]^T \in \mathbb{R}^n, \quad (2.1)$$

which is subjected to constraints:

$$\begin{aligned} g_j(x) &\leq 0, \quad j = 1, 2, \dots, m, \\ h_j(x) &= 0, \quad j = 1, 2, \dots, m. \end{aligned}$$

The Newton method uses a second order approximation of $f(x)$ to evaluate the optimum point. The approximation can be defined as:

$$f(x_k + \Delta x) \approx f(x_k) + \Delta f(x_k)^T \Delta x + \frac{1}{2} \Delta x^T B \Delta x \quad (2.2)$$

In the Quasi-Newton method, the Hessian is evaluated approximately where Δf is the gradient of f , and B is an approximation of the Hessian.

2.1.1 Adjoint-based Sensitivity Analysis

Gradients of an objective function may be evaluated in different methods. These methods can be classified as direct and adjoint methods. The adjoint method is the

inverse technique in which the gradients of objective functions are calculated for the design variables. The results obtained from the adjoint method is the sensitivity, and hence, it is called as the adjoint-based sensitivity analysis. The adjoint-based sensitivity represents the response of the objective function to the surface deformation. The adjoint method is an effective method, since it is independent of the number of design variables.

The adjoint method conventionally is divided into two, which are called discrete and continuous adjoint methods. In the continuous adjoint approach, adjoint equations are derived from the governing PDEs and then discretized. In the discrete adjoint approach, the adjoint equations are directly derived from the discretized governing equations. The discrete adjoint approach is used in the present study due to its cost effectiveness.

The sensitivity of the numerical residual of the flow equations revaluation with respect to a defined design parameter ζ can be written as:

$$\frac{dR}{d\zeta} = \frac{\partial R}{\partial U} \frac{dU}{d\zeta} + \frac{\partial R}{\partial \zeta} = 0, \quad (2.3)$$

where U is the flow variables, and R is the residual equations. Rearranging the equation with respect to $\frac{dU}{d\zeta}$ gives:

$$\frac{dU}{d\zeta} = - \left(\frac{\partial R}{\partial U} \right)^{-1} \frac{\partial R}{\partial \zeta} \quad (2.4)$$

Let J be the sensitivity of the objective function. Similarly;

$$\frac{dJ}{d\zeta} = \frac{\partial J}{\partial U} \frac{dU}{d\zeta} + \frac{\partial J}{\partial \zeta} \quad (2.5)$$

The substitution of Eq. 2.4 into Eq. 2.5 gives,

$$\frac{dJ}{d\zeta} = - \frac{\partial J}{\partial U} \left(\frac{\partial R}{\partial U} \right)^{-1} \frac{\partial R}{\partial \zeta} + \frac{\partial J}{\partial \zeta} \quad (2.6)$$

Finally, the adjoint equation can be expressed as:

$$\left(\frac{\partial R}{\partial U} \right)^T \Psi = - \left(\frac{\partial J}{\partial U} \right)^T \quad (2.7)$$

In this method, the adjoint matrix, Ψ , is computed by solving the equation (Eq. 2.7). Consequently, the gradient value of the objective function can be written as:

$$\frac{dJ}{d\zeta} = \Psi^T \frac{\partial R}{\partial \zeta} + \frac{\partial J}{\partial \zeta} \quad (2.8)$$

One has to solve the linear system for each objective function. Because the flow field is a discretized volume, flow variables and residual equations are a function of grid coordinates X .

$$\frac{dJ}{dX} \frac{dX}{d\zeta} = \left(\Psi^T \frac{\partial R}{\partial X} + \frac{\partial J}{\partial X} \right) \frac{dX}{d\zeta} \quad (2.9)$$

The sensitivity of design variables at each grid nodes for design variables and the sensitivity derivatives of the objective function corresponding to grid nodes are evaluated separately. Then, the sensitivity derivatives of the objective function for design variables are obtained by Eq.2.9. In the adjoint method, the evaluation of the partial derivatives is required for flow variables, residual functions, and objective functions. The automatic differentiation method, which is based on the systematic application of the differentiation by chain rule, is employed to obtain these partial derivatives.

2.1.2 Surface Parametrization

The optimization problems contain design variables that control variation on shapes. The baseline design is parametrized by providing a Free Form Deformation (FFD) Box, which involves required design variables for the optimization process. For shape optimization problems, multiple design variables can be utilized to define a shape. These variables are described with the nodes that are located on the surface of the FFD box. In this study, different parametrizations using the FFD Box are applied. The first one is parametrized the baseline geometry for the variation in the sweep angle, and the second one is the parametrization of the baseline geometry to control the leading-edge shape deformation.

2.1.2.1 Free Form Deformation Box

In the present study, parametrization of the geometry is carried out with a Free Form Deformation, FFD, Box. The FFD box is a six faced box. It has a meshed structure, like a structured mesh block, which has nodes on the faces with (i, j, k) indices. The variation in the surface geometry is controlled with these nodes in Figure 2.1 .

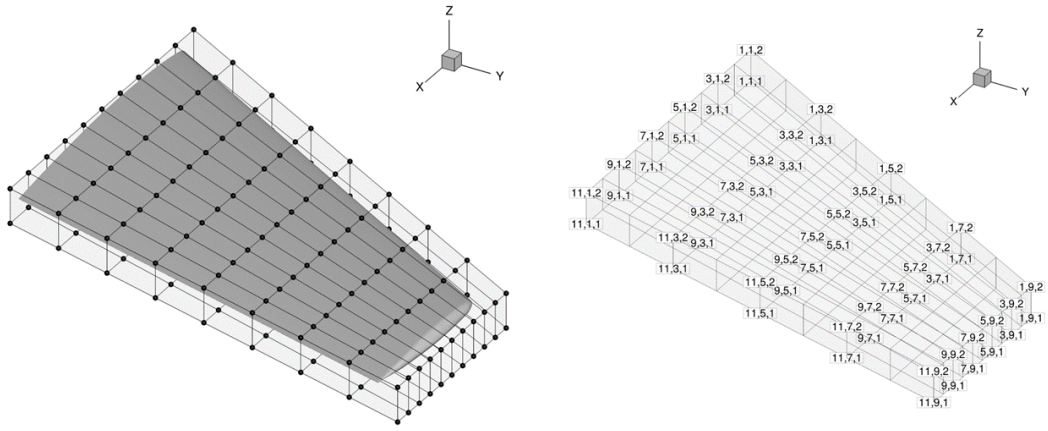


Figure 2.1: View of the FFD Box Enclosing a Wing Including Control Points

The number of control points in each direction is the required polynomial degree. An FFD Box can describe the surface of any formulation or degree, and it is not affected by the domain or mesh used to discretize them. This method is unique such that it automatically deforms the computational grids around (or within) the boundary by deforming the entire volume around (or inside) the boundary. This is considered as a useful feature for automation of design optimization procedures.

The Bezier curve formulation is employed in the grid deformation resulting from a variation in the FFD Box. The Cartesian coordinates of indices (i, j, k) are parametrized by using ξ, η, ς in the degree of l, m, n .

$$X(\xi, \eta, \varsigma) = \sum_{i=0}^l \sum_{j=0}^m \sum_{k=0}^n P_{i,j,k} B_i^l(\xi) B_j^m(\eta) B_k^n(\varsigma) \quad (2.10)$$

$$\begin{cases} B_i^l(\xi) = \frac{l!}{i!(l-i)!} \xi^i (1-\xi)^{l-i} \\ B_j^m(\eta) = \frac{m!}{j!(m-j)!} \eta^j (1-\eta)^{m-j} \\ B_k^n(\varsigma) = \frac{n!}{k!(n-k)!} \varsigma^k (1-\varsigma)^{n-k} \end{cases} \quad (2.11)$$

2.2 SU²: Flow Solver

The SU² is an software package that is capable of solving PDE systems on unstructured meshes. It is developed in the Aerospace Design Lab of Stanford University. The SU² includes several modules. The flow field can be solved with SU2_CFD module. Flow simulations can be obtained by solving either the Euler equations or Reynolds-Averaged Navier-Stokes (RANS) equations. The SU² suite can also provide sensitivity information for surface geometry with respect to grid coordinates with discrete adjoint solver, SU2_CFD_AD, available with the distribution. The gradient projection module, SU2_DOT_AD, performs dot product operation to obtain gradients of the objective function with respect to design variables by using sensitivity information. SU² has also surface deformation module, SU2_DEF, which has capable of the FFD Box parametrization. high-level python scripts are available such as PDE-constraint optimization script In the SU², sciPy.

The solution of a general PDE system given by:

$$\frac{\partial U}{\partial t} + \Delta \cdot \vec{F}^c(U) - \Delta \cdot \vec{F}^v(U) = Q \quad in \Omega \quad (2.12)$$

U : Vector of state variables

$\vec{F}^c(U)$: Convective fluxes

$\vec{F}^v(U)$: Viscous fluxes

$Q(U)$: Generic source term

The motion of fluid flow is described by the Navier-Stokes equations. The instantaneous quantities in the Navier-Stokes equations are decomposed into time-averaged

and fluctuating turbulent quantities. Therefore, the Reynolds Averaged Navier-Stokes, RANS, equations are obtained by means of a turbulence model. If the viscous terms are neglected, the Euler equations are obtained. Numerical solutions of Euler equations and the corresponding adjoint equations are, in general, obtained more efficiently relative to RANS equations.

RANS equations are expressed in terms of the following conservative variables:

$$U = \begin{pmatrix} \rho \\ \rho v_x \\ \rho v_y \\ \rho v_z \\ \rho E \end{pmatrix} \quad (2.13)$$

Where ρ is the density, E is the total energy per unit mass, and $\vec{v} = \{v_x, v_y, v_z\}^T \in R^3$ is the flow velocity in the Cartesian coordinate system. For the SU² RANS solver, the convective fluxes, the viscous fluxes, and the source term are given:

$$\vec{F}_x^c = \begin{pmatrix} \rho v_x \\ \rho v_x^2 + P \\ \rho v_x v_y \\ \rho v_x v_z \\ \rho v_x H \end{pmatrix}, \quad \vec{F}_y^c = \begin{pmatrix} \rho v_y \\ \rho v_x v_y \\ \rho v_y^2 + P \\ \rho v_y v_z \\ \rho v_y H \end{pmatrix}, \quad \vec{F}_z^c = \begin{pmatrix} \rho v_z \\ \rho v_x v_z \\ \rho v_y v_z \\ \rho v_z^2 + P \\ \rho v_z H \end{pmatrix} \quad (2.14)$$

$$\begin{aligned}
\vec{F}_x^v &= \left\{ \begin{array}{c} \cdot \\ \tau_{xx} \\ \tau_{xy} \\ \tau_{xz} \\ v_y \tau_{xy} + v_z \tau_{xz} + \mu_{tot}^* C_p \frac{\partial T}{\partial x} \end{array} \right\}, \\
\vec{F}_y^v &= \left\{ \begin{array}{c} \cdot \\ \tau_{xy} \\ \tau_{yy} \\ \tau_{yz} \\ v_x \tau_{xy} + v_z \tau_{yz} + \mu_{tot}^* C_p \frac{\partial T}{\partial y} \end{array} \right\}, \\
\vec{F}_z^v &= \left\{ \begin{array}{c} \cdot \\ \tau_{xz} \\ \tau_{yz} \\ \tau_{zz} \\ v_x \tau_{xz} + v_y \tau_{yz} + \mu_{tot}^* C_p \frac{\partial T}{\partial z} \end{array} \right\}
\end{aligned} \tag{2.15}$$

Where P is the static pressure, H is the fluid enthalpy. The viscous stresses can be expressed as $\tau_{ij} = \mu_{tot}^* (\frac{\partial v_i}{\partial j} + \frac{\partial v_j}{\partial i} - \frac{2}{3} \delta_{ij} \nabla \cdot \vec{v})$ by recalling i, j indices represents 3-D Cartesian coordinates and $\delta_{i,j}$ symbolizes the Kronecker delta function. In the presentation of formulas of fluxes, C_p is the specific heat at constant pressure where R is the specific gas constant for an ideal gas:

$$C_p = \frac{\gamma R}{\gamma - 1} \tag{2.16}$$

T is the temperature, and where the equation of state is following as:

$$T = \frac{P}{R\rho} \tag{2.17}$$

One can close the system by determining pressure form:

$$P = \frac{(\gamma - 1)\rho}{E - 0.5(\vec{v} \cdot \vec{v})} \tag{2.18}$$

Additionally, viscosity term in Eq.2.19 indicates:

$$\mu_{tot}^* = \frac{\mu_{dyn}}{Pr_d} + \frac{\mu_{tur}}{Pr_t} \quad (2.19)$$

The dynamic viscosity, μ_{dyn} , is evaluated by Sutherland's law, and the turbulent viscosity μ_{tur} is obtained from a suitable turbulence model involving the mean flow state U and a set of new variables for the turbulence, which are discussed comprehensively in the next section. Moreover, Pr_d and Pr_t are the dynamic and turbulent Prandtl numbers, respectively.

For the stability constraints in adjoint equations, the one-equation Spalart-Allmaras turbulence model is employed. It is designed for aerospace applications involving wall-bounded flows [68]. The model uses the actual minimum distance of a field point to the nearest wall, and it can work with both unstructured and structured grids. The Spalart-Allmaras model solves a modeled transport equation to evaluate the turbulent viscosity as follows;

$$\begin{aligned} \frac{\partial \hat{\nu}}{\partial t} + v_j \frac{\partial \hat{\nu}}{\partial x_j} = & c_{b1}(1 - f_{t2})\hat{S}\hat{\nu} - \left[c_{w1}f_w - \frac{c_{b1}}{\kappa^2}f_{t2} \right] \left(\frac{\hat{\nu}}{d} \right)^2 + \\ & \frac{1}{\sigma} \left[\frac{\partial}{\partial x_j} \left((\nu + \hat{\nu}) \frac{\partial \hat{\nu}}{\partial x_j} \right) + c_{b2} \frac{\partial \hat{\nu}}{\partial x_i} \frac{\partial \hat{\nu}}{\partial x_i} \right] \end{aligned} \quad (2.20)$$

and turbulent viscosity equation is;

$$\mu_t = \rho \hat{\nu} f_{v1}, \quad (2.21)$$

where $f_{v1} = \frac{\chi^3}{\chi^3 + c_{v1}^3}$, $\chi = \frac{\hat{\nu}}{\nu}$ whereby $\nu = \mu/\rho$ describes kinematic viscosity. Additional equations are given;

$$\hat{S} = \Omega + \frac{\hat{\nu}}{\kappa^2 d^2 + c_{v1}^3} f_{v2}. \quad (2.22)$$

Ω describes vorticity, $\Omega = \sqrt{2W_{ij}W_{ij}}$ and d is the distance between field point and the nearest wall. The parameters, in the turbulence model, are described as;

$$\begin{aligned} f_{v2} &= 1 - \frac{\chi}{\chi f_{v1} + 1} \\ f_w &= g \left[\frac{1 + c_{w3}^6}{g^6 + c_{w3}^6} \right] \end{aligned}$$

$$\begin{aligned}
g &= r + c_{w2}(r^6 - r) \\
r &= \min \left[\frac{\hat{\nu}}{\hat{S}\kappa^2 d^2}, 10 \right] \\
f_{t2} &= c_{t3} e^{-c_{t4} \chi^2} \\
W_{ij} &= \frac{1}{2} \left[\frac{\partial v_i}{\partial x_j} - \frac{\partial v_j}{\partial x_i} \right],
\end{aligned}$$

where i, j are indices describing Cartesian coordinates. The boundary conditions and constants are;

$$\begin{aligned}
\hat{\nu}_{wall} &= 0, & \hat{\nu}_{farfield} &= 3\nu\infty : to : 5\nu\infty \\
c_{b1} &= 0.1355 & \sigma &= \frac{2}{3} & c_{b2} &= 0.622 & \kappa &= 0.41 \\
c_{w2} &= 0.3 & c_{w3} &= 2 & c_{v1} &= 7.1 & c_{t3} &= 1.2 \\
c_{t4} &= 0.5 & c_{w1} &= \frac{c_{b1}}{\kappa^2} + \frac{1 + c_{b2}}{\sigma}
\end{aligned}$$

2.2.1 Solution of the Discrete Adjoint Equations

SU² has a builtin discrete adjoint solver. The solution of the discrete adjoint equation follows the computation of the partial derivatives given in Eq. 2.7. If the adjoint variables in Eq. 2.7 are obtained, the derivative of the objective function with respect to grid coordinates can be evaluated by Eq. 2.23.

$$\frac{dJ}{dX} = \Psi^T \frac{\partial R}{\partial X} + \frac{\partial J}{\partial X} \quad (2.23)$$

The discrete adjoint solver needs Jacobian matrices and the partial derivatives of the objective function which are already computed by the SU2_CFD module. Once the matrices and vectors are constructed, the adjoint system is solved by an iterative solver.

2.2.2 Boundary Conditions

The SU² has the following boundary conditions:

- no-slip wall boundary condition (adiabatic and isothermal),
- far-field as free-stream condition,
- Euler and symmetry conditions,
- near-field boundaries,
- inlet boundary conditions such as fixed mass flow, static pressure, and velocity,
- outlet boundary conditions such as back pressure, and mass flow,
- periodic boundary condition.

For the solution of RANS equations the following boundary conditions are used:

- no-slip wall boundary condition, adiabatic and isothermal is applied
- free-stream conditions are applied to the semi-sphere far-field surrounding of domain
- symmetry condition is applied to the plane splits the aerodynamic body

2.2.3 Solver Setup

The SU² has the following linear solvers:

- The Flexible Generalized Minimal Residual (FGMRES) method,
- The Biconjugate Gradient Stabilized (BCGSTAB) method.

The following flux splitting methods are applicable in the code:

- Jameson-Schmidt-Turkel's (JST) central scheme,
- ROE upwind scheme,
- HLLC upwind scheme.

The Flexible Generalized Minimal Residual (FGMRES) method linear solver is used to solve the implicit problem and Jameson-Schmidt-Turkel's central second-order scheme is used for numerical convective fluxes .

2.3 Grid Generation

The computational grids are generated via the Pointwise grid generation software. Hybrid unstructured grids with prismatic cells in the boundary layer zones are employed throughout the study. The surface grids are generated by considering the aspect ratio of the cells, that can not exceed 3, and the growth ratio of grids' edges is limited to 1.11 to remain the smooth transition. Triangular surface grids are used to generate the triangular prisms in the boundary layer zones. The first layer of the boundary layer is set to approximately $y^+ = 1$ value, and the viscous layer is meshed up to the sufficient boundary height, which is based on flat-plate boundary layer theory. Outside the boundary layer zones tetrahedral cells are created. The farfield volume is designed as a half-sphere, and it is about ten times the model length. Three different grids are generated by controlling the growth ratio of the edges, which are 1.1, 1.2, and 1.3 in the direction normal to the surface. It should be noted that SU² is a node-based finite volume flow solver.

2.3.1 Solution Adaptive Grids

The SU² code is capable of the solution adaptive grid refinement methodology. It performs the refinement based on the density gradient. The methodology is implemented based on the suggested technique by Biswas and Strawn [69], which uses an an-isotropic grid refinement technique. The density gradient based refinement significantly improves the accuracy of the predictions in vortex dominated [70, 71].

2.4 Optimization Algorithm

The optimization process is driven by the open source optimization software DAKOTA [72]. DAKOTA is an open-source optimization tool kit, which is developed by Sandia National Laboratories. It includes a variety of gradient-based optimizations algorithms.

In the present study two optimization cases are considered. The first one is the leading edge shape in a strake-wing configuration, and the second one is the optimization for

the sweep angle of the strake. The optimization algorithm is shown in Figure 2.2.

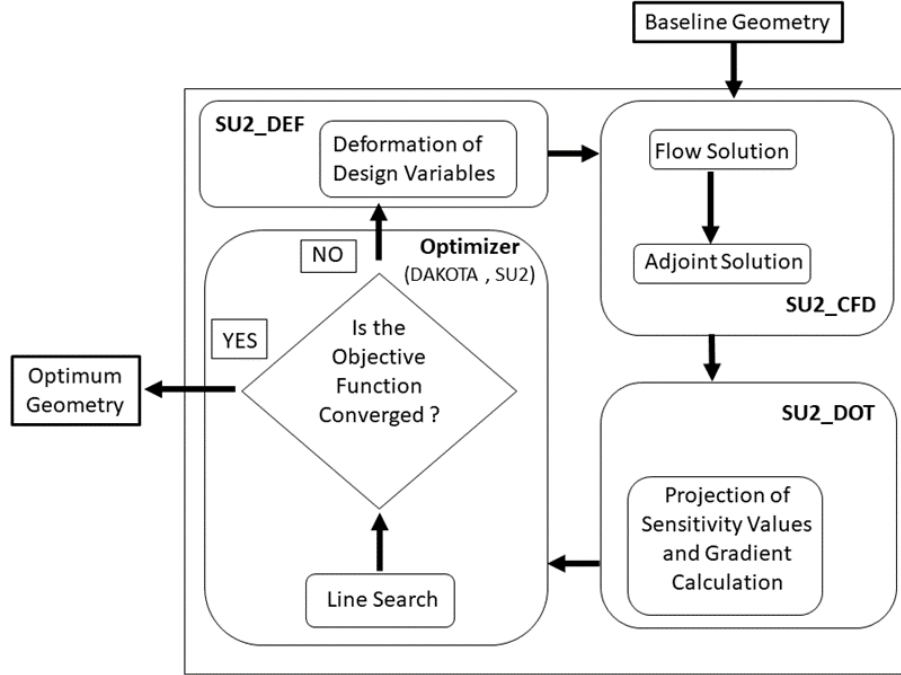


Figure 2.2: Optimization Flowchart

In both cases, the parametrization of the aerodynamic surfaces is performed by FFD Box method. The flow solutions and the aerodynamic efficiency of the current configuration are obtained by SU2_CFD module. Then, the discrete adjoint solver SU2_CFD_AD, computes the grid sensitivities of the objective function. Finally, the gradients are calculated by performing the projection of the grid sensitivities onto the design variables, which are the control points on the FFD boxes. DAKOTA software drives the search process in order to find the optimum design variables in the design space by using the gradients. Once the design variables are updated, SU2_DEF performs the deformation of the configuration and the computational grid for the next design step. The optimization cycle continues until the convergence criteria is satisfied.

CHAPTER 3

RESULTS AND DISCUSSION

In this chapter, the flow solutions with SU^2 over the reference strake-delta wing configuration [41] are first verified on solution adaptive grids. The adjoint-based aerodynamic shape optimizations are then performed at 10° and 22.5° angles of attack. At 10° , a profile optimization based on inviscid flow solutions is also performed. The results obtained are presented in detail and discussed.

3.1 Reference Study

The experimental study performed by Verhaagen et al. [41] on a delta strake-wing configuration shown in Figure 3.1 is taken as a reference study. The sweep angles of the strake and the wing are 76° and 40° , respectively. The experiments are performed at 10° angle of attack, and a Mach number of 0.2 and $Re = 1 \times 10^6$. The spanwise pressure distribution at 75% of the chord and surface oil flow visualizations which show the vortex breakdown locations are available in their technical report.

Verhaagen et al. state that the leading-edge sweep angle and the difference between strake and wing leading edge sweep angles have substantial impacts on the strake and wing vortex interactions and the breakdown of wing vortex in high angle of attack aerodynamics [41]. It is also stated that there is a narrow vortex interaction between strake and wing vortices below the 10° angle of attack, whereas the interactions get stronger as the angle of attack increases.

In the present shape optimization study, two angles of attack cases, $\alpha = 10^\circ$ and 22.5° are considered. Flow solutions with the SU^2 are similarly obtained at a Mach number

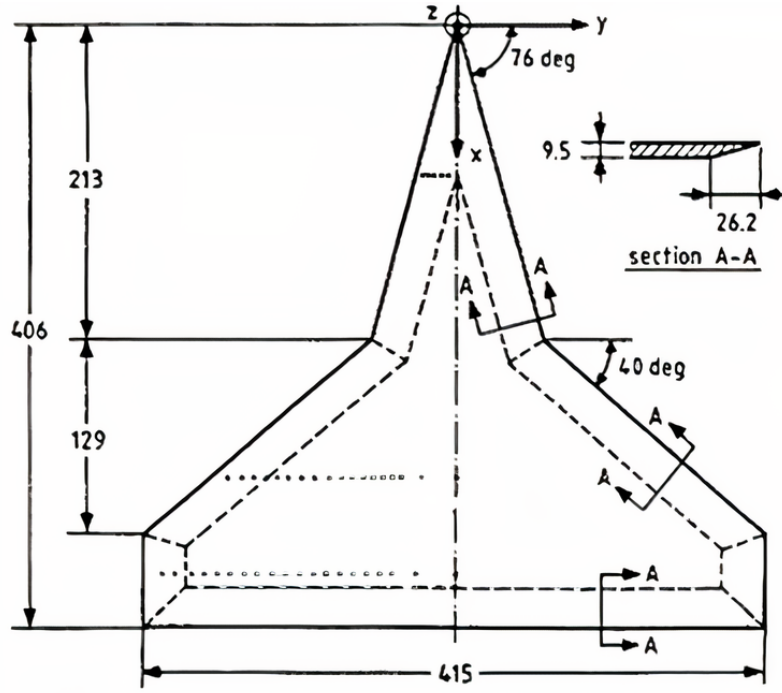


Figure 3.1: Reference Configuration

of 0.2, and $Re = 1 \times 10^6$. Grid independent solutions are obtained first by varying the grid resolutions within the boundary layer zone and then employing adaptive solution grids outside the boundary layer zone.

3.1.1 Computational Grids

In the generation of computational grids, the high-density triangular surface mesh shown in Figure 3.2 is initially generated. The surface grid is then used to extrude the triangular prism cells within the boundary layer zone and the tetrahedral cells in the outer zone, as shown in Figure 3.3. For the inviscid solutions, the solution domain is constructed with tetrahedral cells only. The number of nodes and the number of layers in the boundary layer zones of the grids, which are used in the mesh independency study, are presented in Table 3.1.

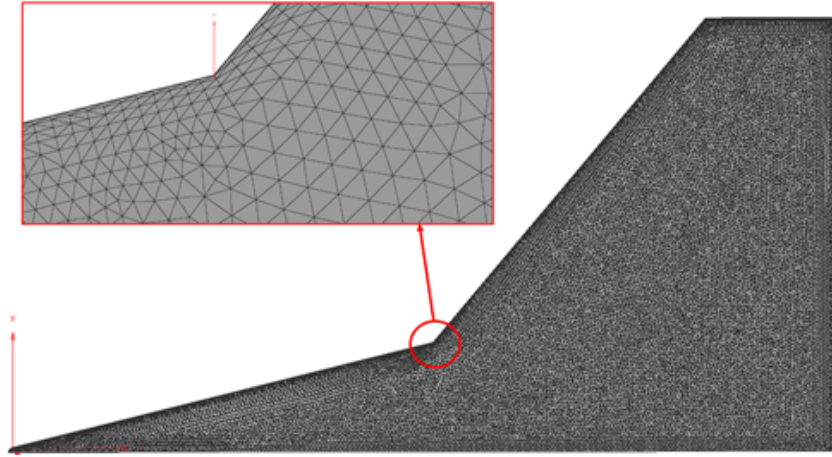


Figure 3.2: Surface Mesh

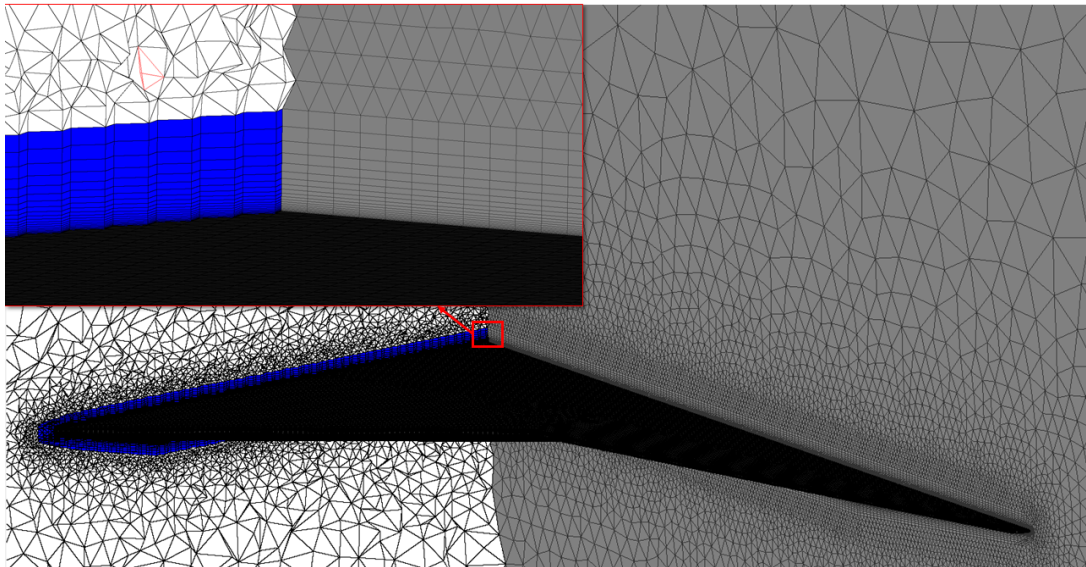


Figure 3.3: Volume Mesh

Table 3.1: Mesh Sizes Used in Mesh Independency Study

Mesh Metrics		
Mesh	Number of Nodes	Number of Layers
Coarse Mesh	0.8 M	25
Medium Mesh	1.6 M	33
Fine Mesh	3.0 M	40

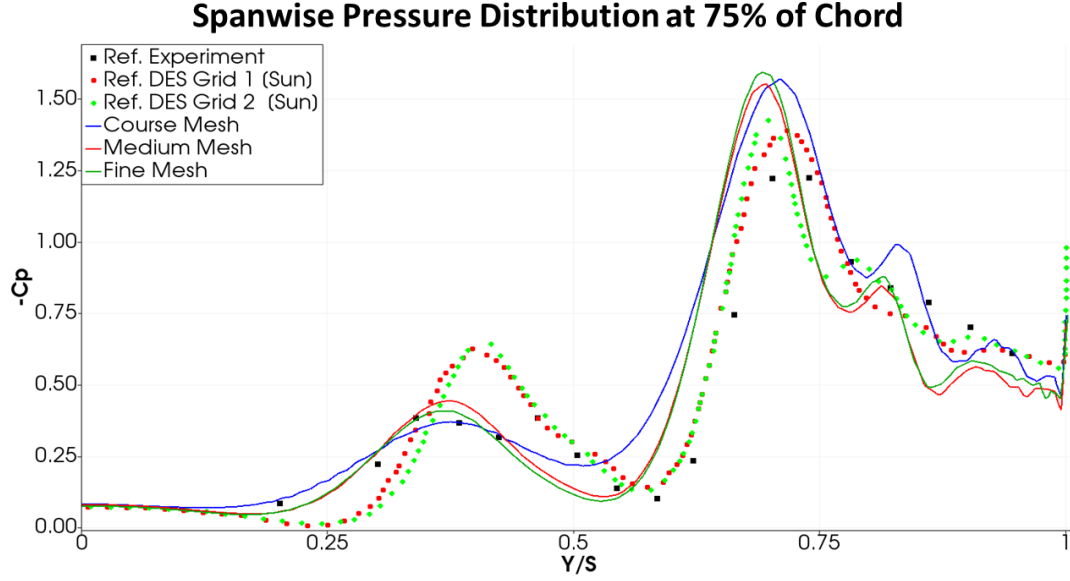


Figure 3.4: Pressure Coefficient Values on Upper Surface along Span

3.1.2 Verification of SU²

The turbulent flows over the baseline strake-wing configuration at $\alpha = 10^\circ$ are computed on the computational grids given in Table 3.1. The assessment of the grid resolutions is based on the comparison of the spanwise pressure distribution at 75% of the chord, as shown in Figure 3.4. Although the present predictions and the reference numerical solutions are not in good agreement with the experimental data, they predict the suction peaks caused by the strake and the wing vortices. Yet, it is seen that the increase in boundary layer resolution leads to a converging behavior in the present predictions. Considering the limited computing resources, the "medium" grid is chosen to be the baseline grid to be employed in the numerical solutions, with the adaptive grid refinement to be performed.

Prior to solutions on adaptive grids, an assessment of Spalart-Allmaras and Menter's Shear-Stress Transport (SST) turbulence models available in SU² is performed. The turbulent flows over the baseline strake-wing configuration at $\alpha = 10^\circ$ are similarly computed on the fine grid. The spanwise pressure distributions at 75% of the chord are shown in Figure 3.5. The L/D ratios obtained with the SA and SST models are 3.633 and 3.605, respectively. In addition, Figure 3.6 shows the vortex breakdown

locations based on the variation of the axial velocity along with the wing vortex core. As observed, both turbulence models predict the vortex breakdown at about 82% wing chord location. Since the SA model is computationally more efficient and known to be more stable in adjoint solutions, it is employed in the remainder of the study.

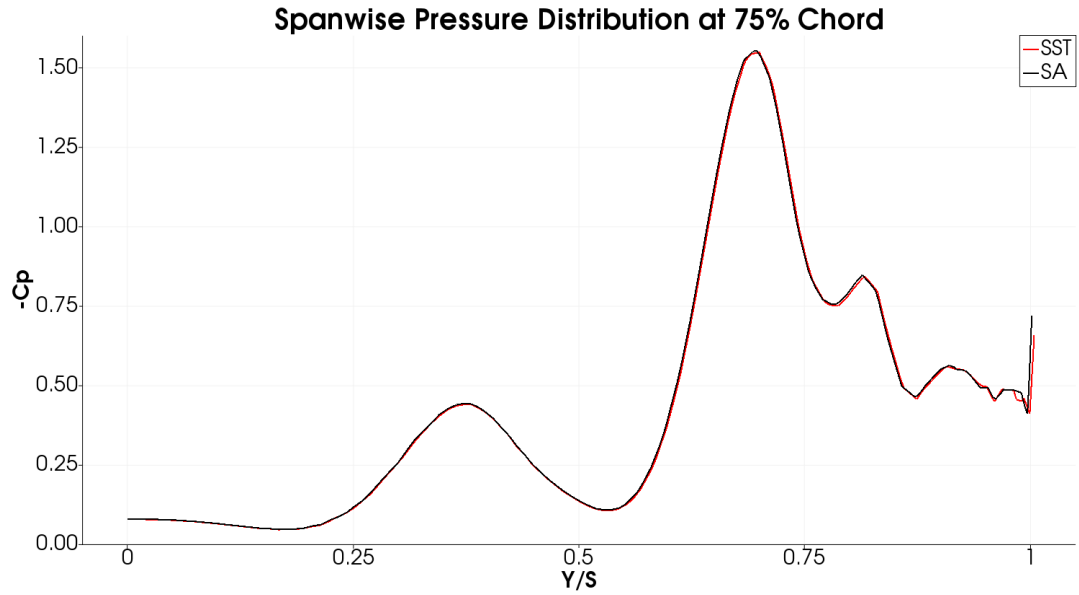


Figure 3.5: Pressure Coefficient Values on Upper Surface along Span

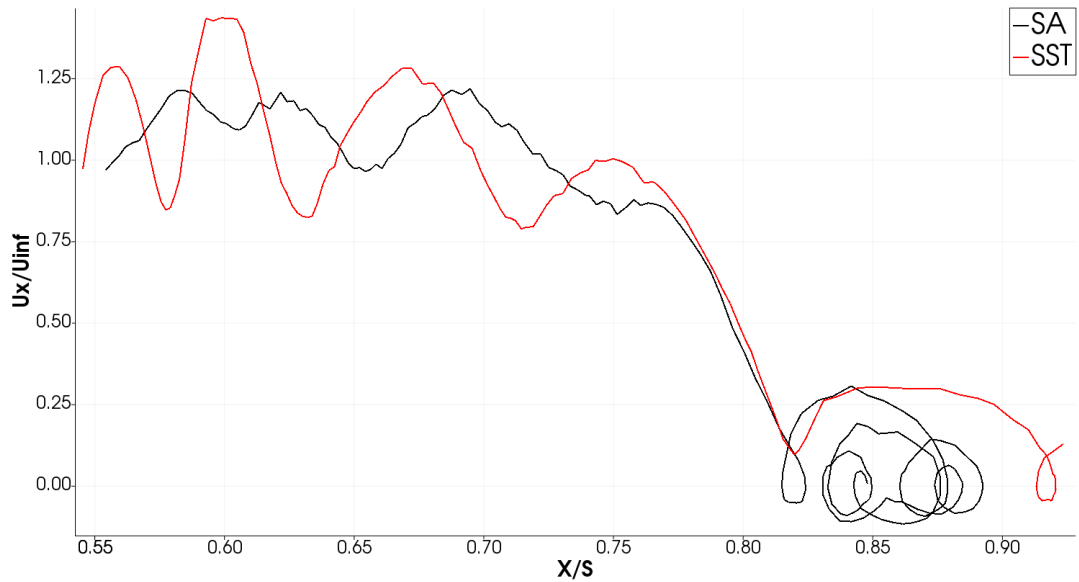


Figure 3.6: Variation of Axial Velocity along Wing Vortex Core

3.1.2.1 Solution Adaptive Grid Refinement

In order to improve the accuracy of the vortical flow solutions and to obtain grid-independent solutions, the solution adaptive grid refinement methodology available in SU² is employed. Tetrahedral cells in the solution domain are adapted three times based on the density gradients computed in the flow field. In each adaptation step, the total number of grid nodes is only allowed to increase by 5%.

Figure 3.7 shows the spanwise pressure distributions computed on the adaptive and fixed grids together with the reference studies. It is observed that the predictions at the 2nd and the 3rd adaptation levels almost overlap, and they are in a much better agreement with the reference DES predictions. Although the prediction of the suction peak due to wing vortex is not improved, the suction peak due to strake vortex is now predicted much stronger as in the DES predictions. It is attributed to the fact that the grid adaptation properly resolves the strake vortex and prevents its numerical diffusion on otherwise a coarser grid.

Table 3.2: Mesh Adaptation Levels

Mesh Metrics	
Mesh	Number of Nodes
Medium Mesh	1.6 M
Adaptation Level 1	1.7 M
Adaptation Level 2	1.8 M
Adaptation Level 3	1.9 M

3.2 Design Variables

There are two different sets of design variables for the two optimization case studies. In the leading edge shape optimization, the design variables, which are the control points of the FFD box, are depicted in Figure 3.8 with bullets. These control points are on the same plane as the strake, and they are only allowed to move in the spanwise direction. The variation of the control points in the spanwise direction controls the shape of the strake leading edge.

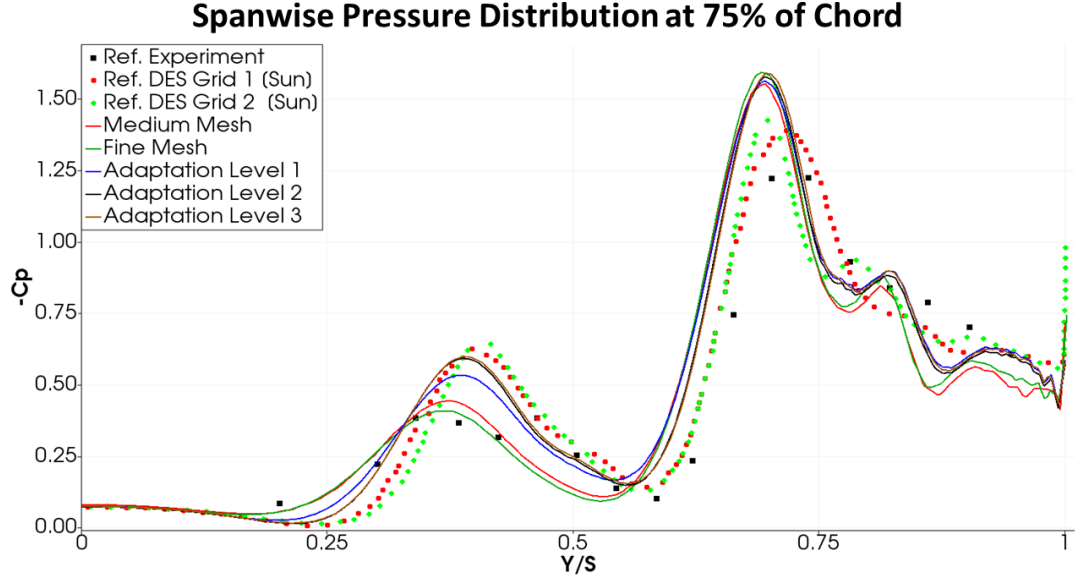


Figure 3.7: Spanwise Pressure Distribution on Upper Wing Surface

In the second case, two contiguous FFD boxes are defined for the optimization of the strake sweep angle. The change in the sweep angle is controlled with the movement of adjacent faces of FFD boxes. The adjacent faces are described with four control points. The reciprocal control points of the two adjacent faces are identical and move together. Consequently, the face movement results from the movement of those points. The control points are only allowed to move along to wing leading and the trailing edges in order to preserve the proper strake-wing connection. The movement of the control points produces the change in the sweep angle as shown in Figure 3.9.

3.3 Aerodynamic Shape Optimization

In this section, results of the shape optimization of the strake geometry are presented and investigated for both 10° and 22.5° angles of attack. The adjoint-based optimizations are performed for both inviscid and viscous flow solutions, and the results are assessed at 10° angle of attack.

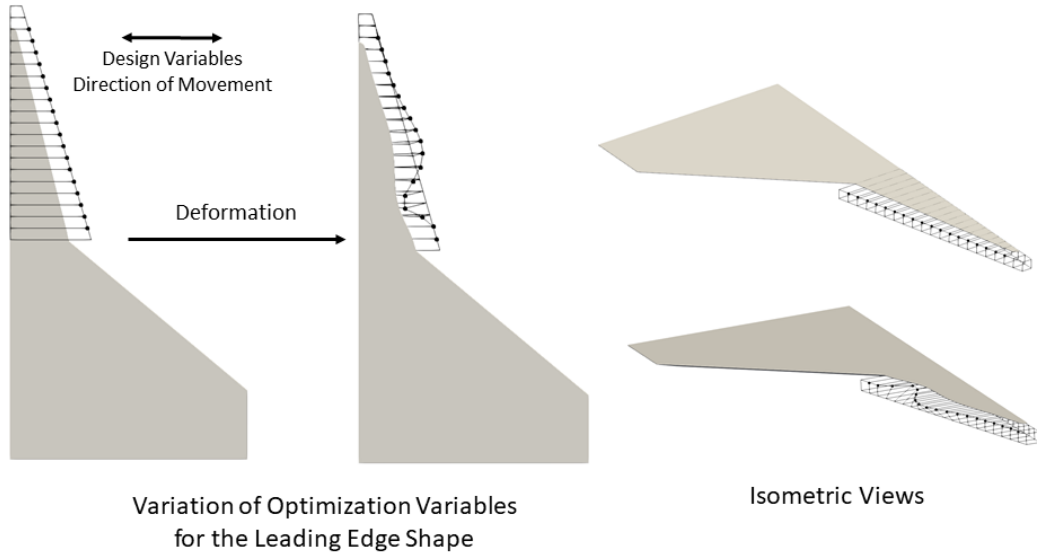


Figure 3.8: Design Variables for Leading Edge Shape Optimization

3.3.1 Shape Optimization at $\alpha = 10^\circ$

The shape optimization of the strake at 10° is performed based on inviscid and viscous flow solutions in order to assess the numerical efficiency and the accuracy of the optimization process based on inviscid flow solutions.

3.3.1.1 Optimization Based on Inviscid Flow Solutions

The solution adapted computational grid for inviscid flow solutions is comprised of 0.25 million nodes. The flow and adjoint solutions take about 0.5 and 0.85 CPU hours using 128 cores, and the DAKOTA-driven optimization process for 12 optimization steps takes about 22.5 CPU hours.

The variation in the objective function and the corresponding leading edge profiles along the optimization process are shown in Figure 3.10 and Figure 3.11. As ob-

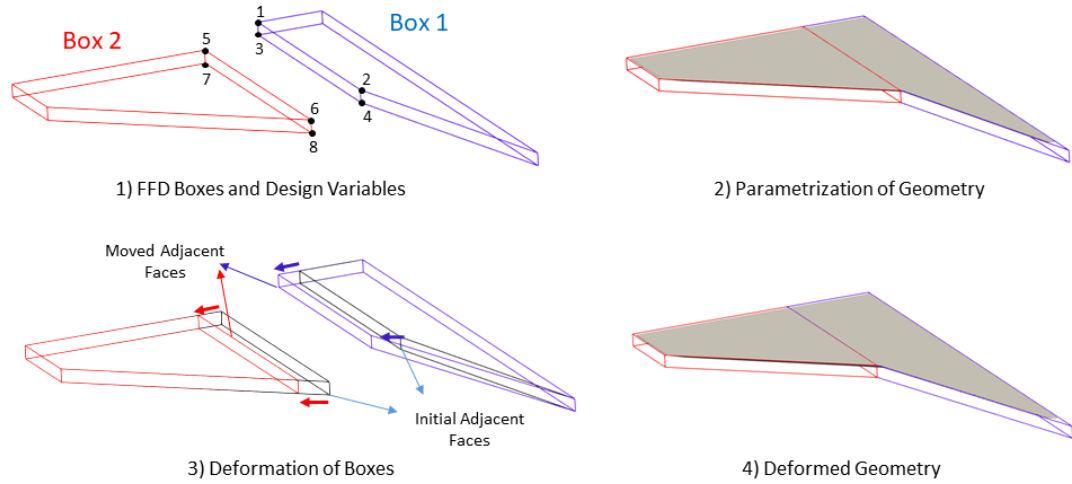


Figure 3.9: Design Variables for the Sweep Angle Optimization

served, the strake shape changes rapidly in the initial steps as the objective function, L/D ratio, increases. At the 12th optimization step, the leading edge profile takes its final form, and the L/D ratio is improved by about 8%.

The turbulent flow field over the optimum shape obtained based on the inviscid solution is next computed, and it is found that the aerodynamic efficiency, L/D ratio, increases only by about 3%.

The turbulent flow fields and the surface pressure distributions for the baseline and the optimum configurations are compared in Figures 3.12, 3.13 and 3.14. The streamlines and the q -criterion contours in Figures 3.13 and 3.14 reveal the fact that the wing vortices have about the same trajectory and breakdown at about the same location over the wing. The surface pressure distributions in Figures 3.12 3.13 indicate that the suction induced by the strake vortex in the optimum configuration is stronger, which is responsible for the increase in lift and the aerodynamic efficiency.

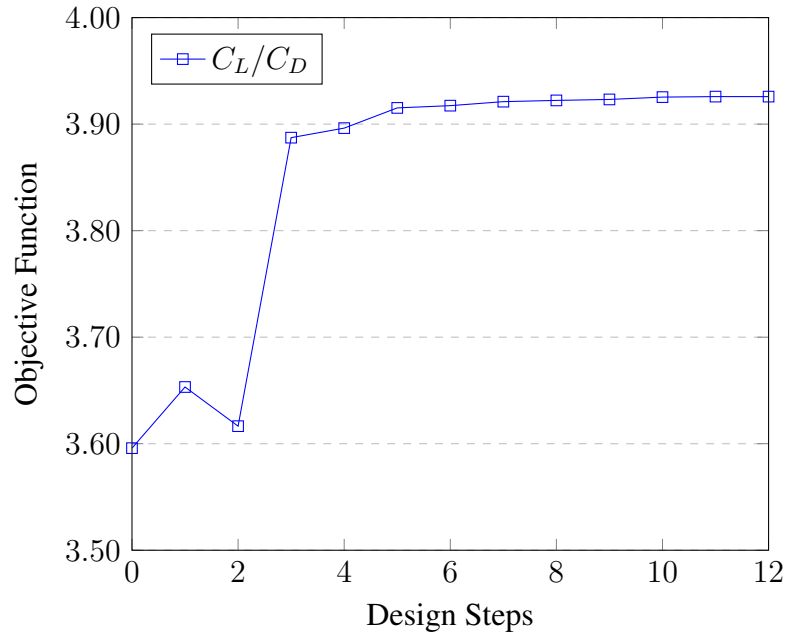


Figure 3.10: Variation of Objective Function at $\alpha = 10^\circ$

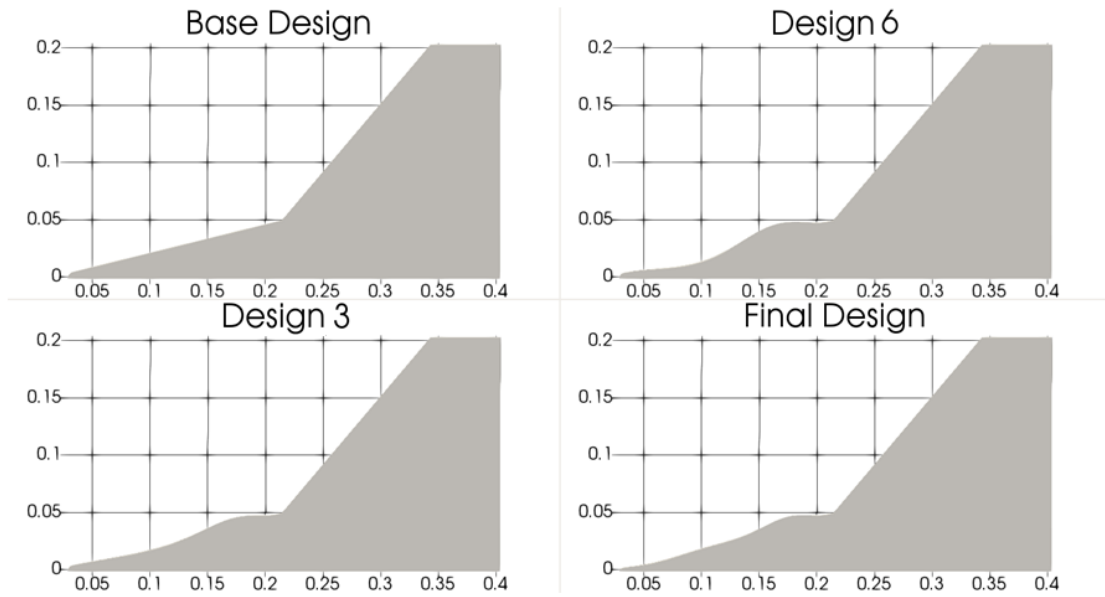


Figure 3.11: Strake Configuration along Optimization Steps at $\alpha = 10^\circ$

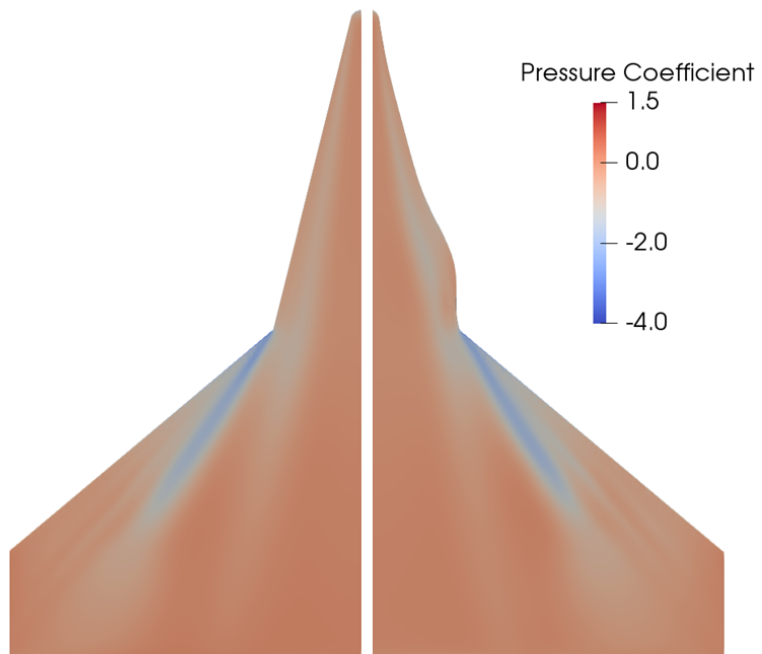


Figure 3.12: Pressure Distribution on Upper Surface at $\alpha = 10^\circ$

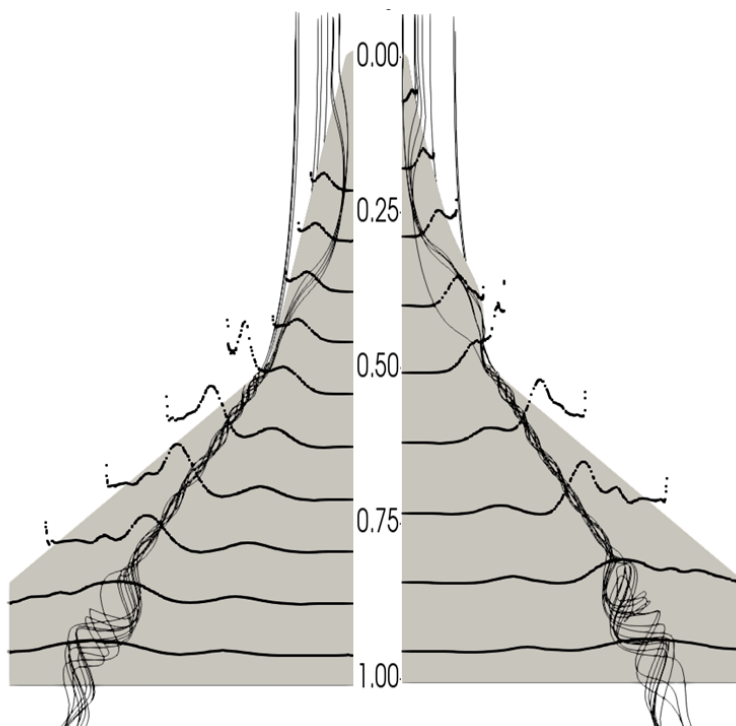


Figure 3.13: Streamlines along Wing Vortex and Spanwise Pressure Plots at $\alpha = 10^\circ$

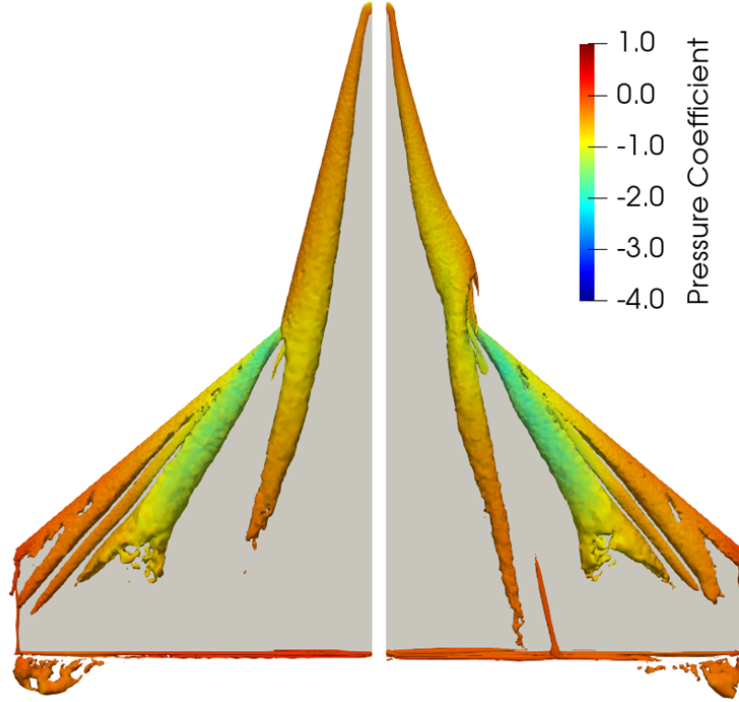


Figure 3.14: Q-criterion Contours and Spanwise Surface Pressure Distributions at $\alpha = 10^\circ$

It is concluded that the shape optimization based on the inviscid flow assumption slightly improves the lift generation due to the stronger strake vortex and the corresponding aerodynamic efficiency but does not prevent the wing vortex breakdown. Next, the same optimization process is repeated for turbulent flows in order to assess further the practicality of the strake shape optimizations with the inviscid flow assumption.

3.3.1.2 Optimization Based on Turbulent Flow Solutions

The solution adapted computational grid for turbulent flow solutions is now comprised of 1.8 million nodes. The flow and adjoint solutions take about 3.3 and 8.48 CPU hours using 512 cores, and the DAKOTA-driven optimization process for 12 optimization steps takes about 85.5 CPU hours. The turbulent flow-based optimization process is about 16 times more expensive than the inviscid flow-based optimization.

The variation in the objective function and the corresponding leading edge profiles

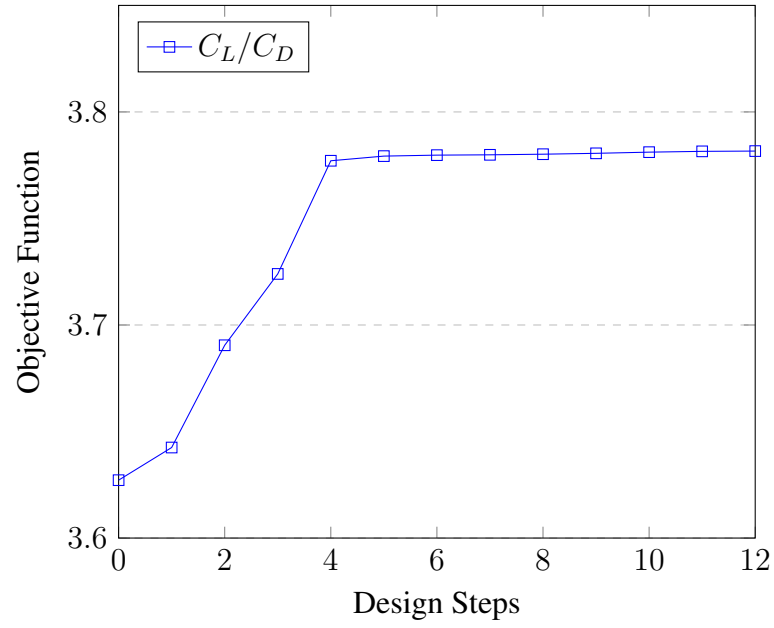


Figure 3.15: Variation of Objective Function at $\alpha = 10^\circ$

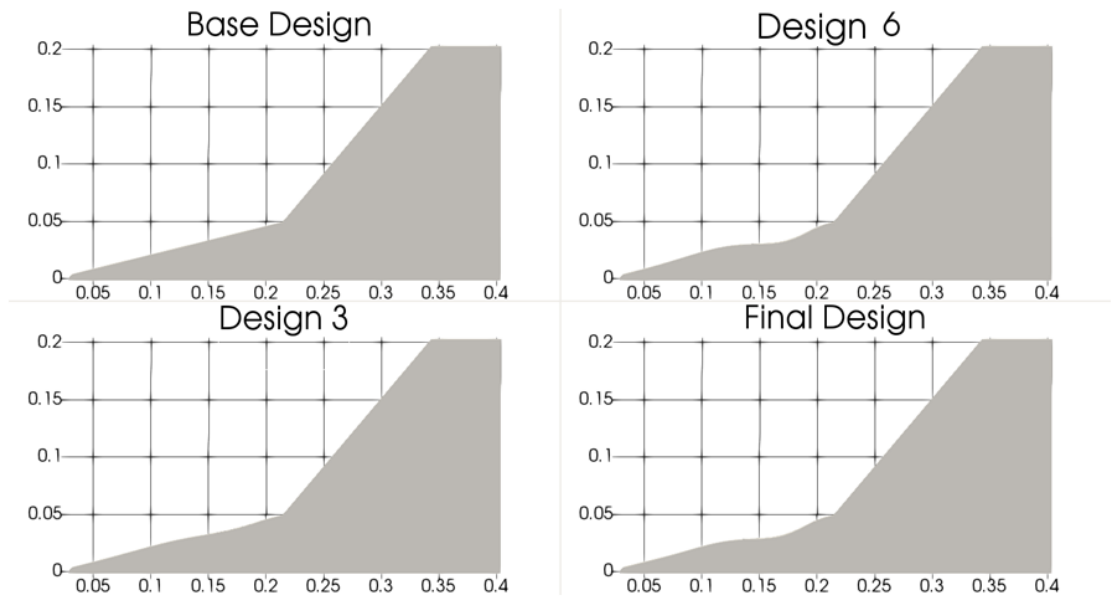


Figure 3.16: Strake Configuration along Optimization Steps at $\alpha = 10^\circ$

along the optimization process are similarly shown in Figure 3.15 and Figure 3.16.

As observed, the optimization process converges to an optimum aerodynamic efficiency value of about 3.78 after about 4th step, which provides an increase by about 4.5%. The strake leading edge profile similarly changes along the optimization steps and converges to an optimum profile which is quite different than the one obtained in the previous inviscid optimization study. In addition, the optimum strake area is not increased as much as it is in the inviscid case.

It should be noted that the improvement in the aerodynamic efficiency is greater than the 3% value, which is achieved earlier based on the inviscid optimization study. Now it can be concluded that aerodynamic shape optimizations to improve the aerodynamic efficiency of strake-delta wing configurations need to be performed with turbulent flow solutions for accuracy at the expense of computational resources.

The comparison of the surface pressure distributions for the baseline and the optimum configurations in Figures 3.17 and 3.18 shows that the suction pressure induced by the wing vortex is stronger in the optimum configuration and it is preserved past the 0.35 wing chord location. The suction induced over the wing by the strake vortex is similarly greater in the optimum configuration. The vortex trajectories given in Figure 3.18 and the q-criterion contours given in Figure 3.19 clearly show that the breakdown of the wing vortex is significantly delayed past the trailing edge. The further inspection of the variation of the axial velocity magnitude in the wing vortex cores given in Figure 3.20 reveals the fact that the wing vortex in the optimum configuration seems not to experience a breakdown over the wing as opposed to the vortex in the baseline configuration. As the vortex breaks down in the baseline configuration, the axial velocity in the vortex core becomes negative, and the vortex core starts recirculating. The axial velocity within the vortex core of the optimum configuration drops but stays positive, which indicates that the complete vortex breakdown is avoided.

3.3.2 Shape Optimization at $\alpha = 22.5^\circ$

Another shape optimization based on turbulent flow solutions is performed at a higher angle of attack, $\alpha = 22.5^\circ$. The variation of the aerodynamic efficiency and the strake

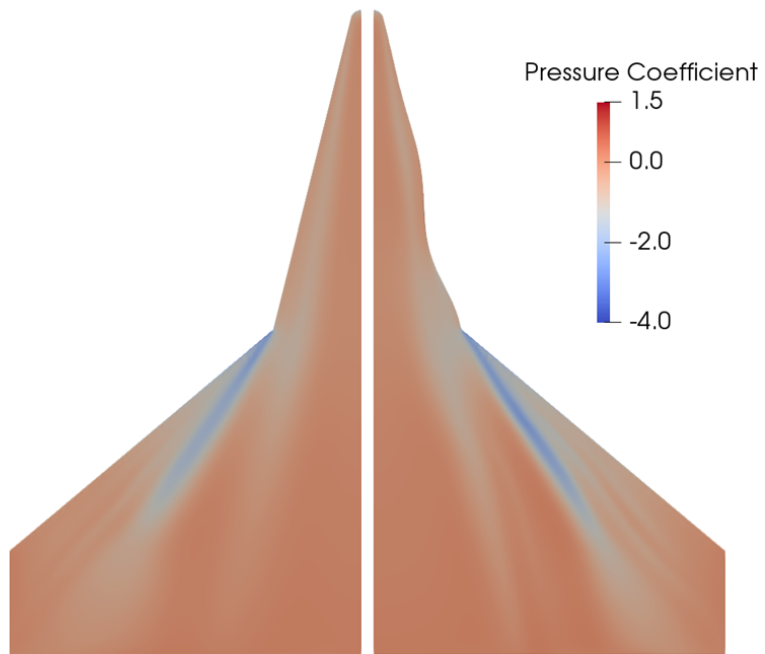


Figure 3.17: Pressure Distribution on Upper Surface at $\alpha = 10^\circ$

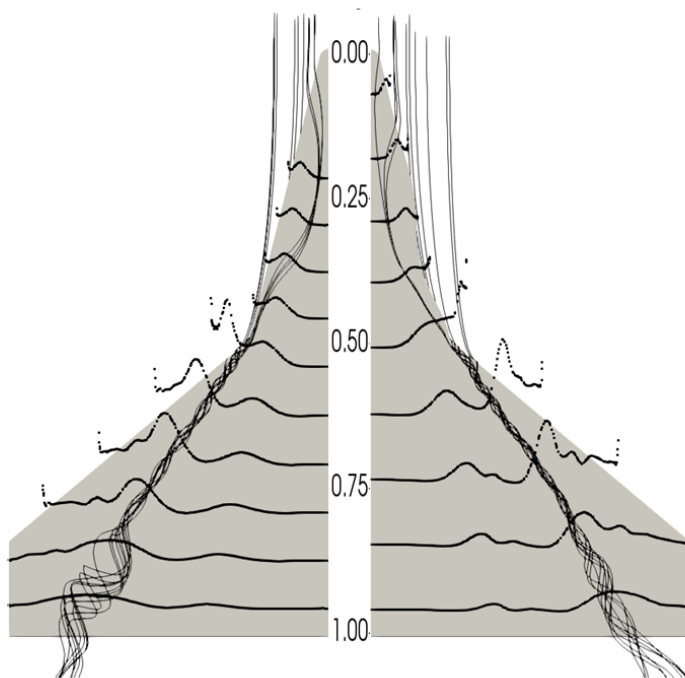


Figure 3.18: Streamlines along Wing Vortex and Spanwise Pressure Plots at $\alpha = 10^\circ$

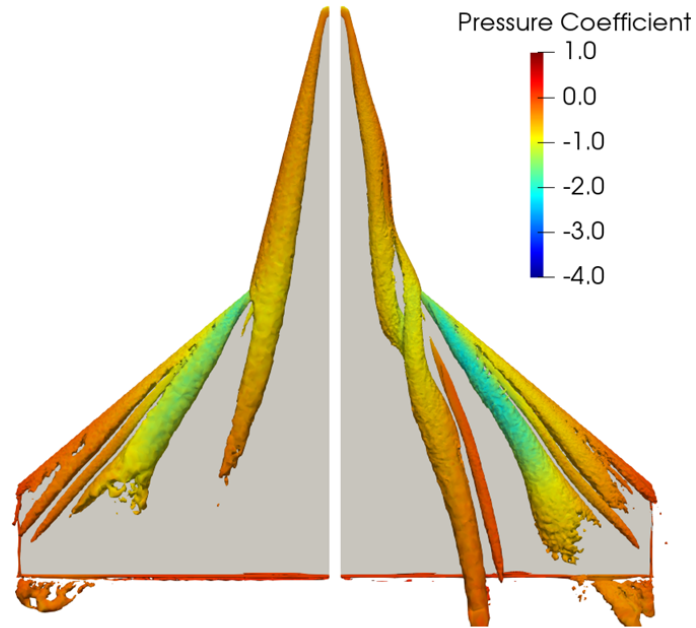


Figure 3.19: Q-criterion Contours and Spanwise Surface Pressure Distributions at $\alpha = 10^\circ$

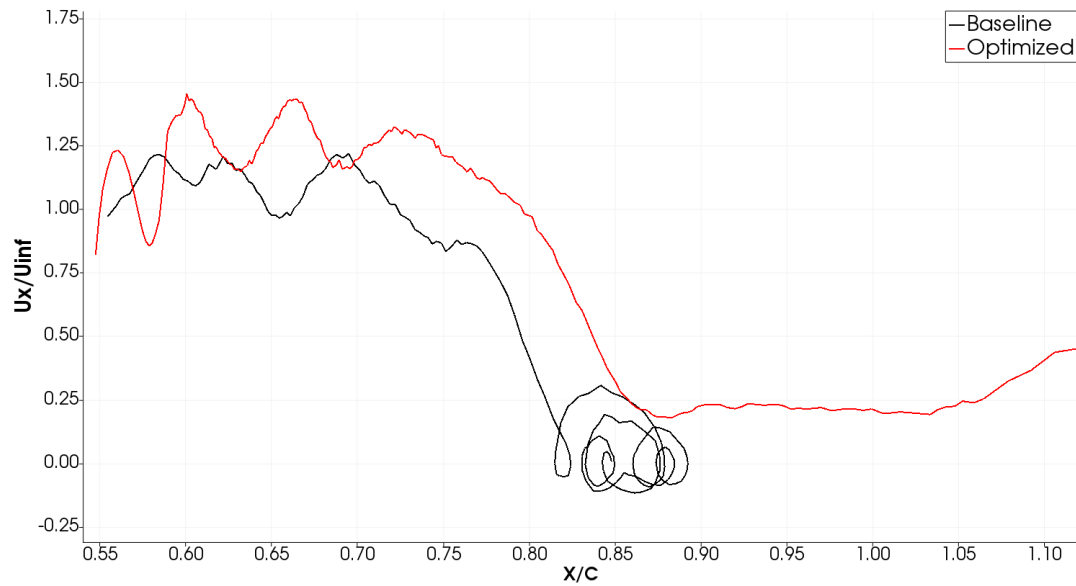


Figure 3.20: Variation of Axial Velocity along Wing Vortex Core at $\alpha = 10^\circ$

shape along the optimization step are given in Figures 3.21 and 3.22, respectively. The optimization process converges almost after the 8th step, and the optimum aerodynamic efficiency only improves by about 3.1% as opposed to 8% obtained earlier at 10° angle of attack case. The optimum strake shape is also observed to be deformed wider close to the apex in comparison to the $\alpha = 10^\circ$ case.

Figure 3.23 and 3.24 show the surface pressure distributions and the wing vortex trajectory. As observed, the optimum configuration produces stronger suction pressures over the strake and the wing, which is attributed to the stronger streak vortex generation and its influence on the wing vortex. The wing vortex is observed to have a tighter core, and the suction it induces extends farther downstream. On the other hand, the q-criterion contours in Figure 3.25 and the variation of axial velocity in the vortex core in Figure 3.26 indicate that the vortex breakdown locations are about the same in the baseline and optimum configurations.

It is concluded that the optimum configuration improves the lift generation over the strake and slightly enhances the lift generation over the wing. As a result, the aerodynamic efficiency improves by 3.1% in comparison to the baseline configuration.

3.4 Sweep Angle Optimization

In this section, only the sweep angle of the strake is optimized while keeping the leading edge straight. Optimizations are performed at 10° and 22.5° angle of attacks. It should be noted that the FFD box employed (Figure 3.9) has two independent control points to be optimized, and their positions are constrained so that they are located on the wing leading and trailing edges.

3.4.1 Sweep Angle Optimization at $\alpha = 10^\circ$

The variation of the aerodynamic efficiency and the change in the sweep angle is given in Figures 3.27 and 3.28. As observed, the optimization process driven by DAKOTA converges after the 4th step as the sweep angle decreases from 76° to 71.6° . The aerodynamic efficiency is improved by 8%.

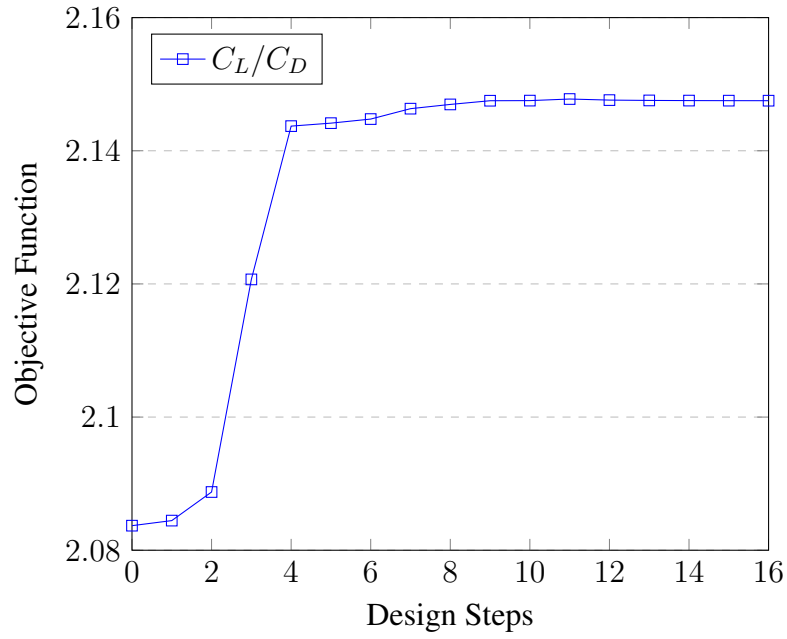


Figure 3.21: Variation of Objective Function at $\alpha = 22.5^\circ$

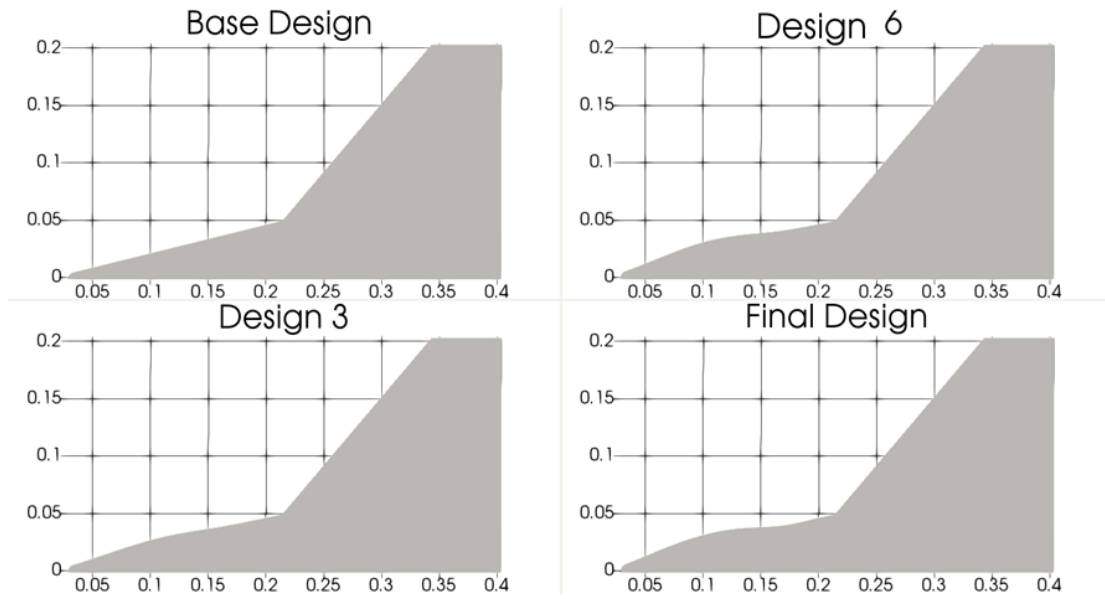


Figure 3.22: Variation of Strake Shape along Optimization Steps at $\alpha = 22.5^\circ$

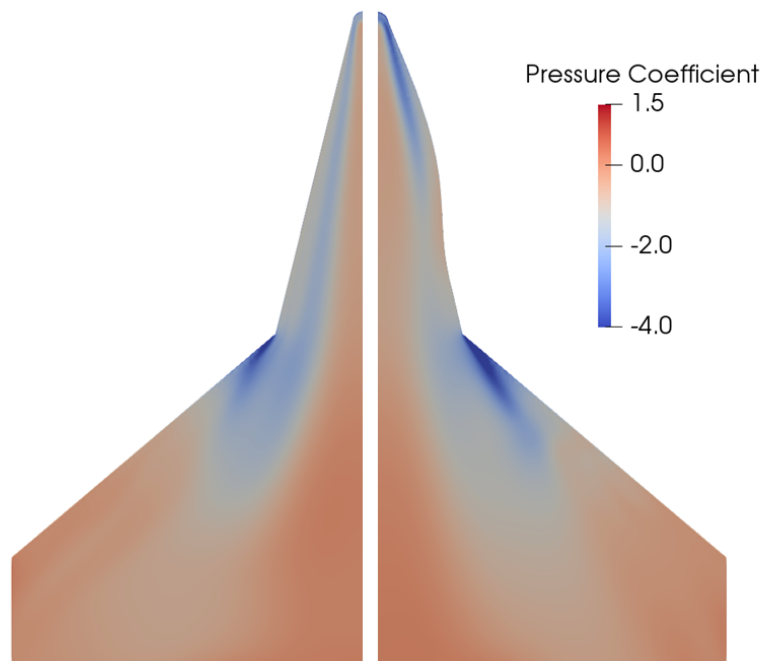


Figure 3.23: Pressure Distribution on Upper Surface at $\alpha = 22.5^\circ$

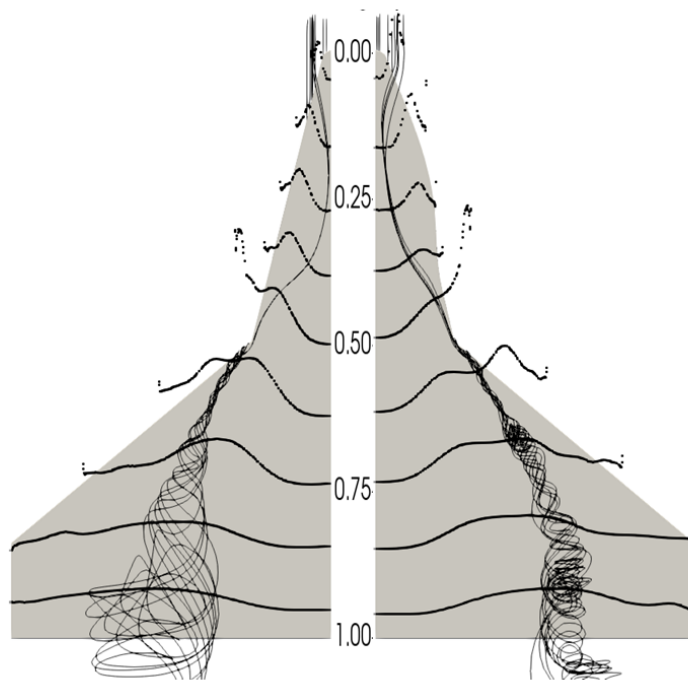


Figure 3.24: Streamlines along Wing Vortex and Spanwise Pressure Plots at $\alpha = 22.5^\circ$

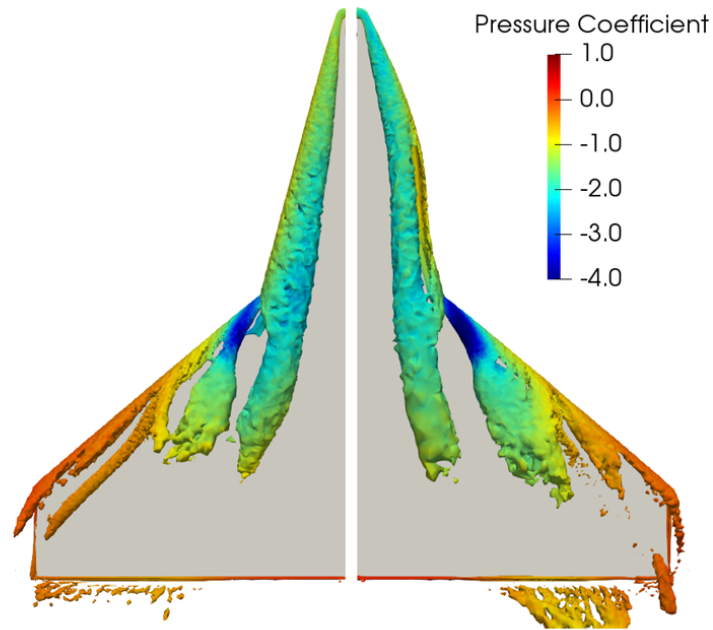


Figure 3.25: Q-criterion Contours and Spanwise Surface Pressure Distributions at $\alpha = 22.5^\circ$

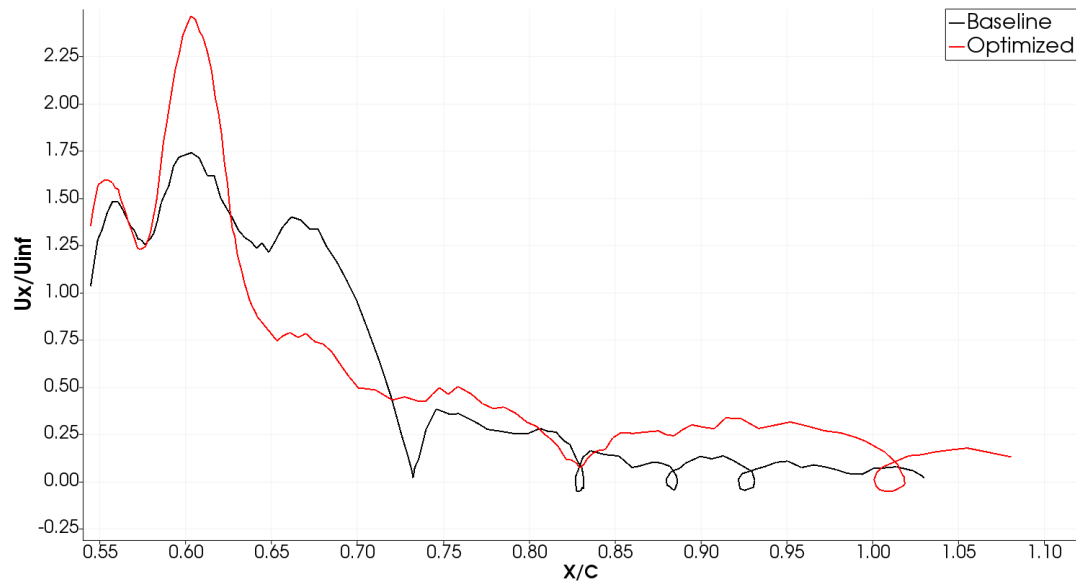


Figure 3.26: Variation of Axial Velocity along Wing Vortex Core at $\alpha = 22.5^\circ$

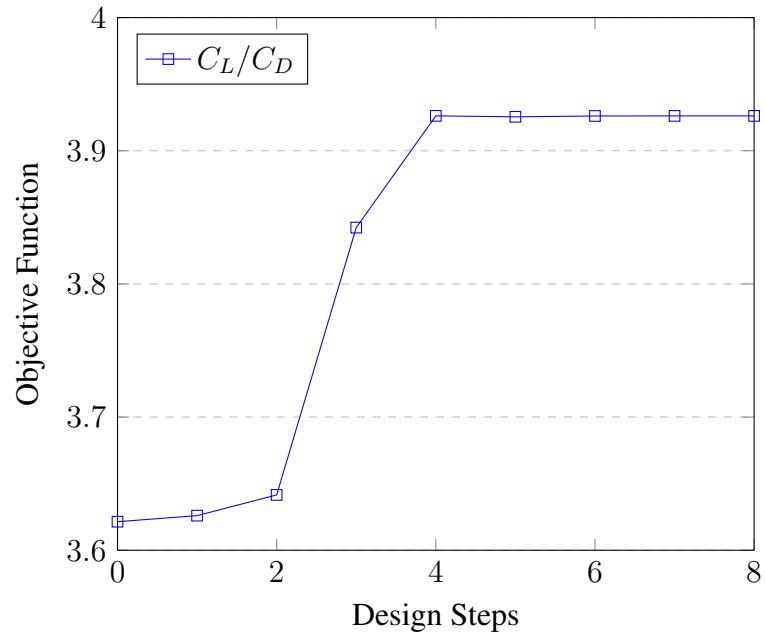


Figure 3.27: Variation of Objective Function at $\alpha = 10^\circ$

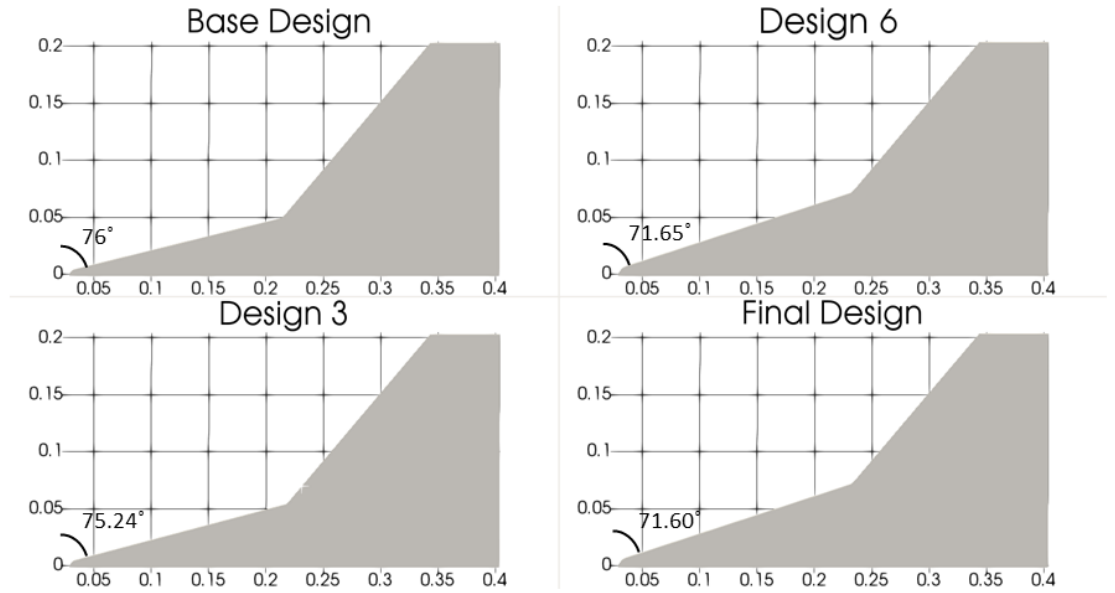


Figure 3.28: Stroke Configuration along Optimization Steps at $\alpha = 10^\circ$

The surface pressure distributions and vortex trajectories for baseline and optimized configurations are similarly compared in Figures 3.29 and Figure 3.30. As observed, the suction induced by the strake vortex over the strake is stronger in the optimum configuration. More significantly, the vortex suction over the wing is sustained till the wing trailing edge.

The streamlines passing through the vortex cores in Figure 3.30, the q-criterion contours in Figure 3.31, and the variation of axial velocity at the vortex core in Figure 3.32 all indicate that the breakdown of the wing vortex observed in the baseline configuration is completely prevented in the optimum configuration. Such a significant increase in the aerodynamic efficiency is achieved by the generation of the stronger strake vortex as a result of the reduced sweep angle and its enhancing influence on the wing vortex.

3.4.2 Sweep Angle Optimization at $\alpha = 22.5^\circ$

The sweep angle optimization is next performed at the 22.5° angle of attack. The optimization process is similarly observed in Figures 3.33 and 3.34. The objective function now behaves more oscillatory along with the optimization steps, and the convergence takes more steps. In the end, the aerodynamic efficiency is improved by about 2.7%, and the sweep angle converges from 76° to 72° . Comparisons of the surface pressure distributions (Figures 3.35 and 3.36) the q-contours (Figure 3.37) and the variation of the axial velocity at the wing vortex core (Figure 3.38) all indicate that the breakdown of the wing vortex is again prevented as a result of the optimization process. At the optimum sweep angle found, the strake vortex becomes stronger, and its coupling with the wing vortex delays its breakdown past the trailing edge. As seen in Figure 3.38, the axial velocity in the vortex core never becomes negative as it does in the baseline configuration.

In order to assess the optimum configurations obtained at the end of all the optimization studies performed in the present study, the spanwise pressure distributions at the 75% of the chord are compared against the baseline configuration in Figure 3.39. It is observed that in the shape optimization cases, the suction pressures induced on the wing surface by both the strake and the wing vortices are enhanced. In the sweep

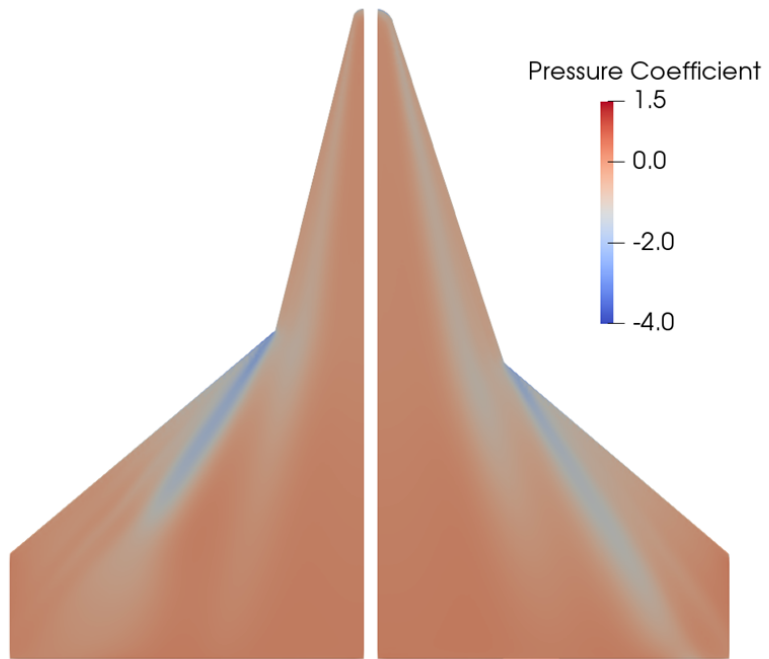


Figure 3.29: Pressure Distribution on Upper Surface at $\alpha = 10^\circ$

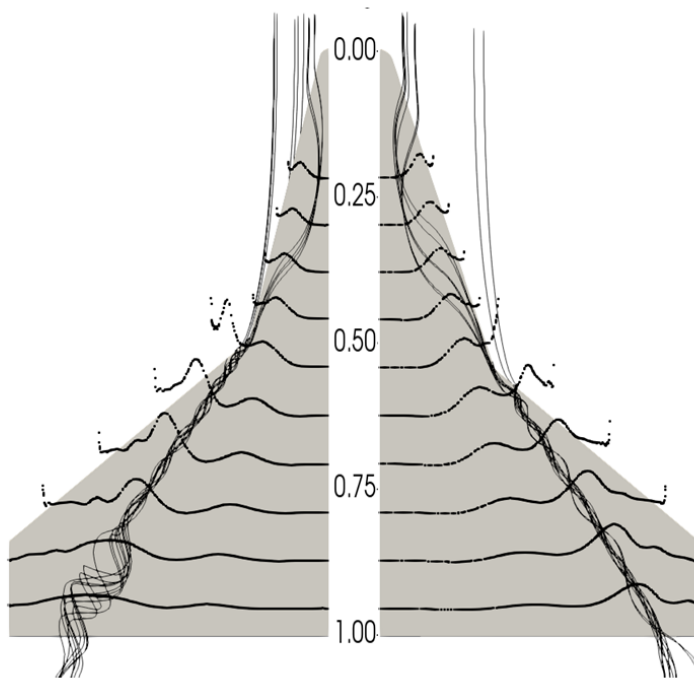


Figure 3.30: Streamlines along Wing Vortex and Spanwise Pressure Plots at $\alpha = 10^\circ$

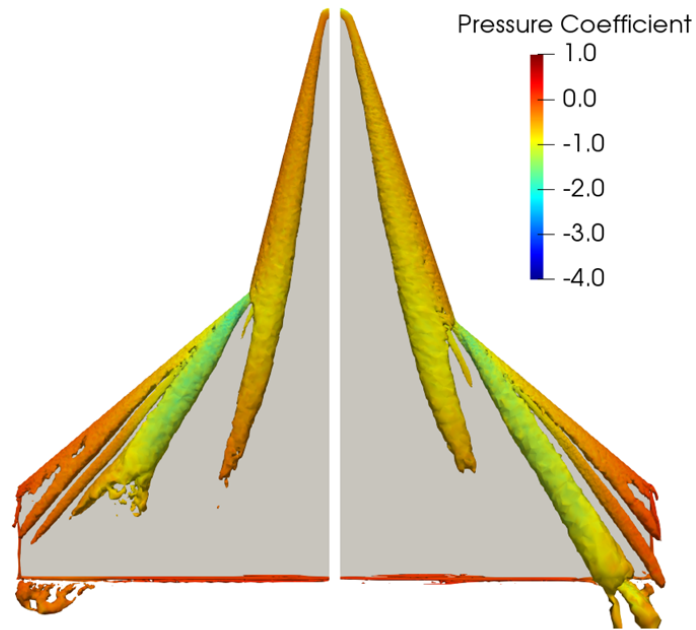


Figure 3.31: Q-criterion Contours and Spanwise Surface Pressure Distributions at $\alpha = 10^\circ$

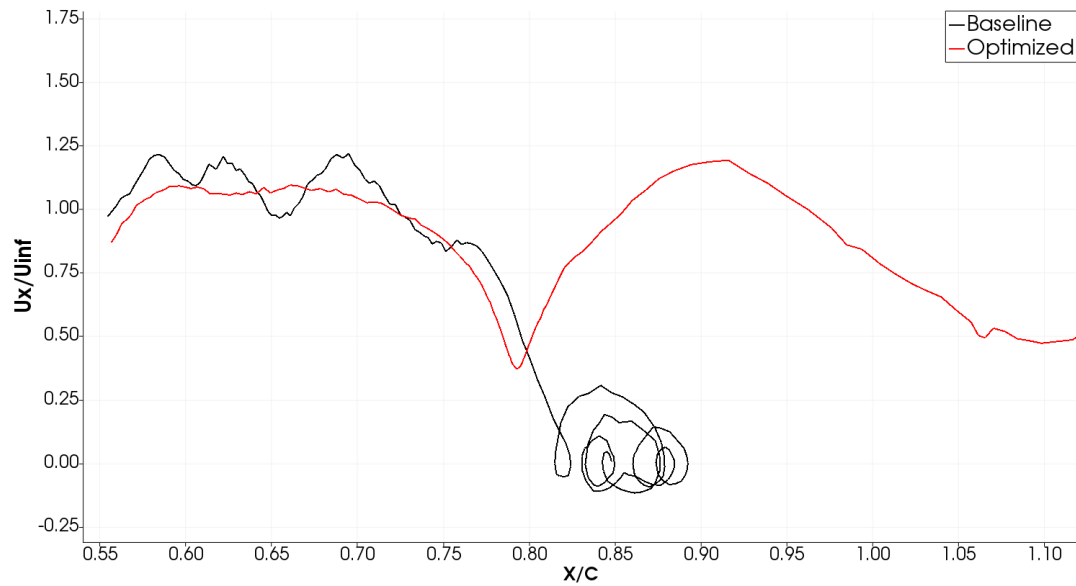


Figure 3.32: Variation of Axial Velocity along Wing Vortex Core at $\alpha = 10^\circ$

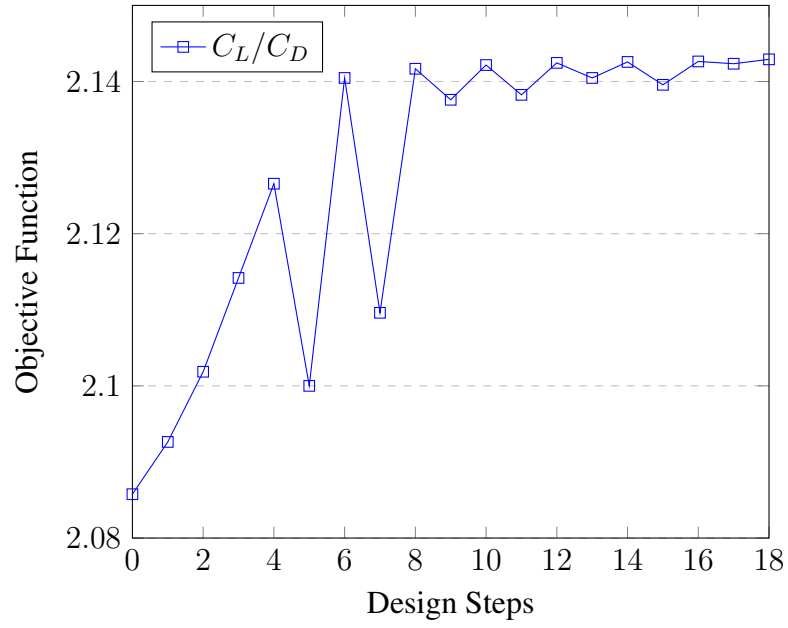


Figure 3.33: Variation of Objective Function at $\alpha = 22.5^\circ$

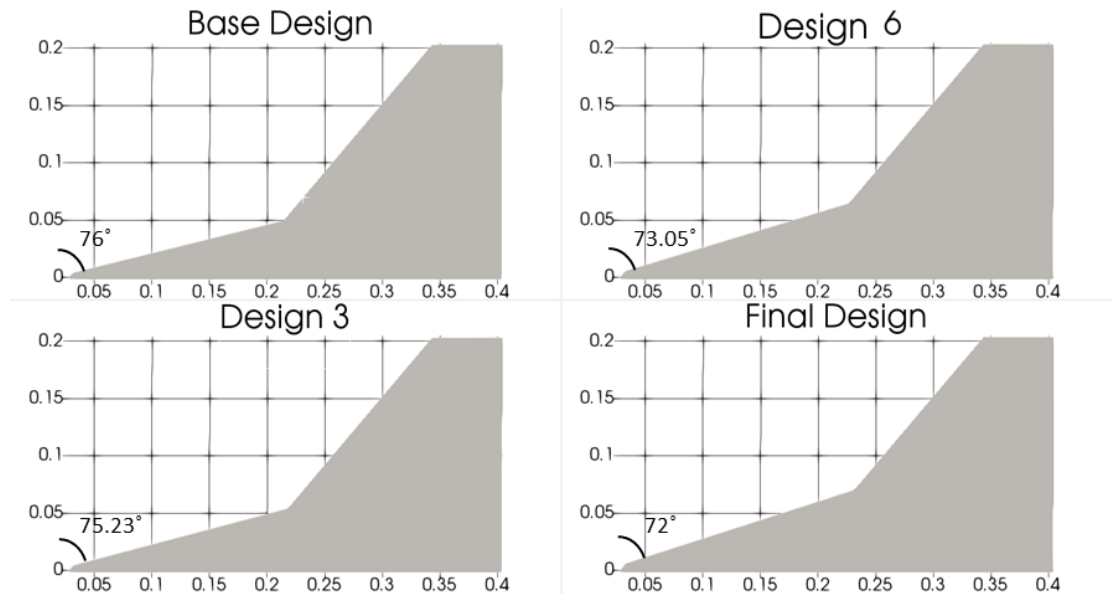


Figure 3.34: Strake Configuration along Optimization Steps at $\alpha = 22.5^\circ$

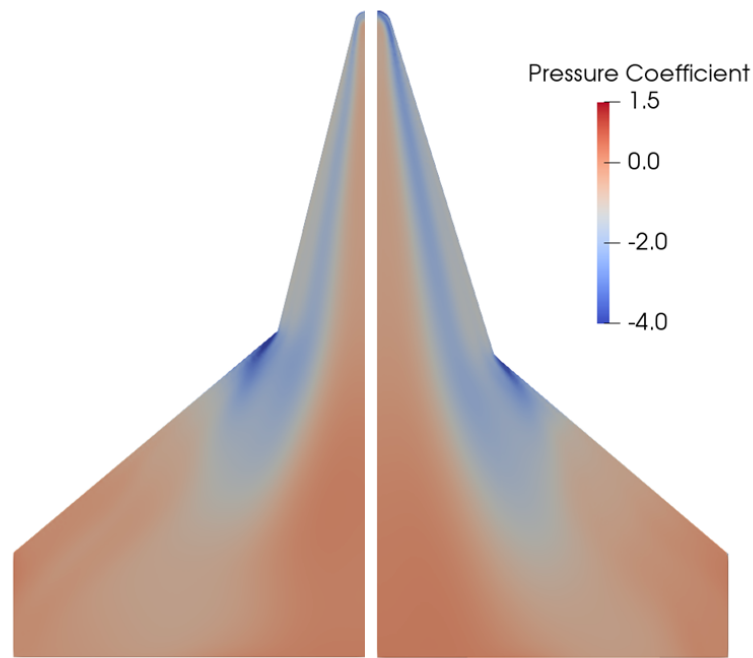


Figure 3.35: Pressure Distribution on Upper Surface at $\alpha = 22.5^\circ$

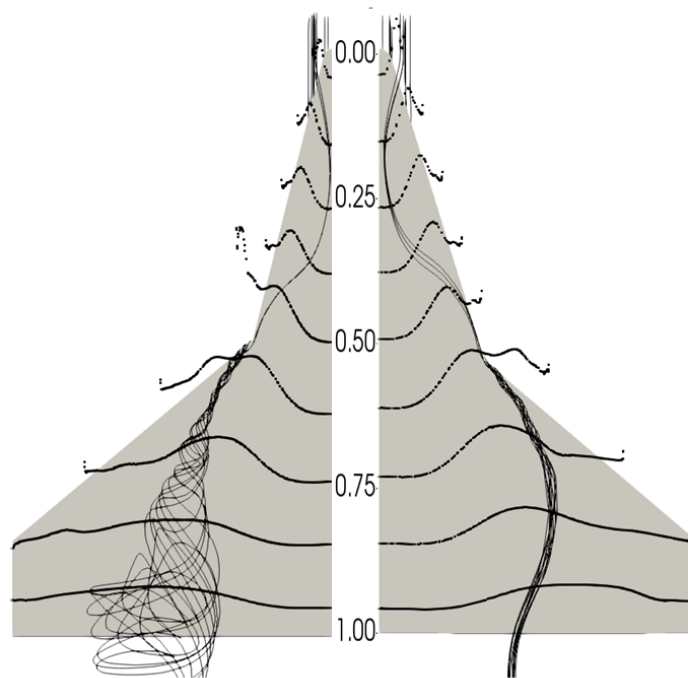


Figure 3.36: Streamlines along Wing Vortex and Spanwise Pressure Plots at $\alpha = 22.5^\circ$

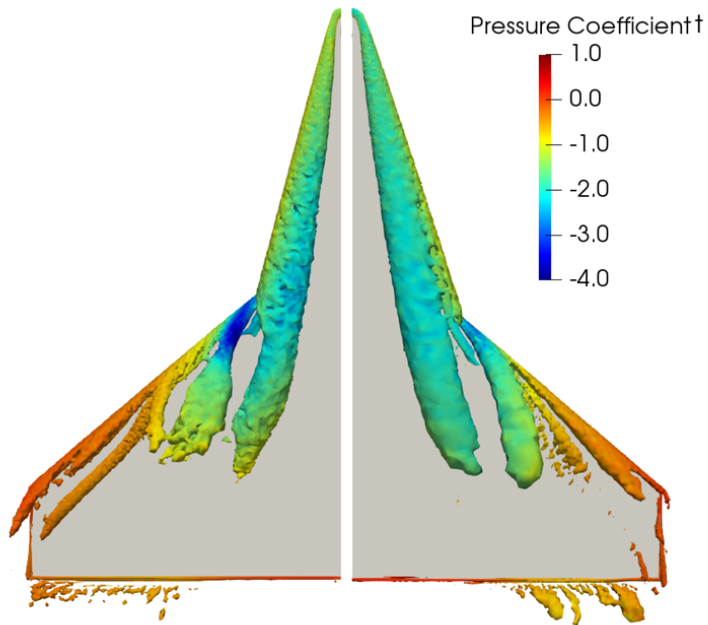


Figure 3.37: Q-criterion Contours and Spanwise Surface Pressure Distributions at $\alpha = 22.5^\circ$

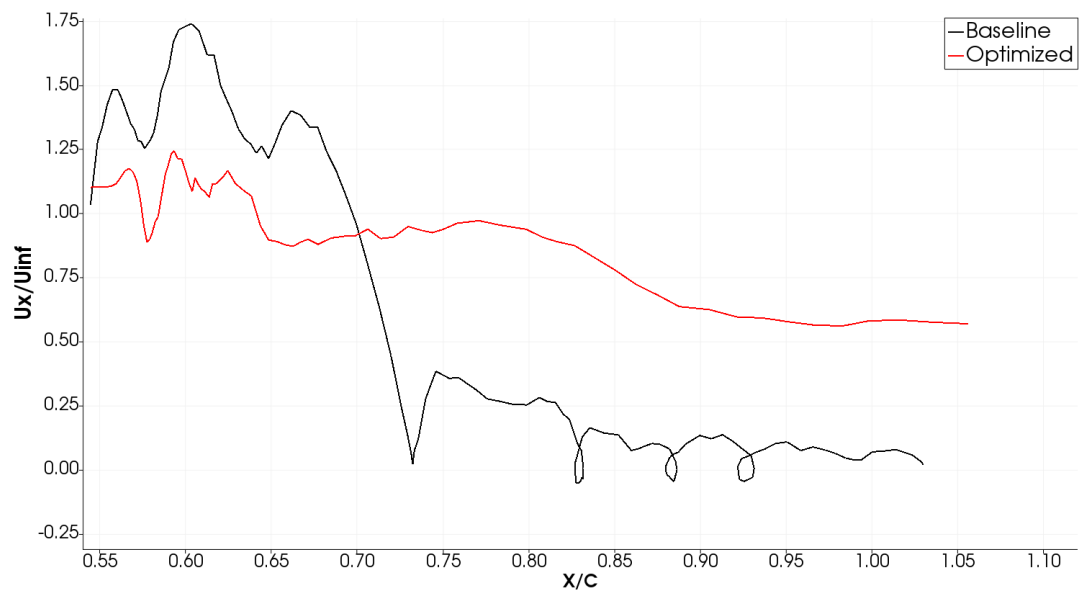


Figure 3.38: Variation of Axial Velocity along Wing Vortex Core at $\alpha = 22.5^\circ$

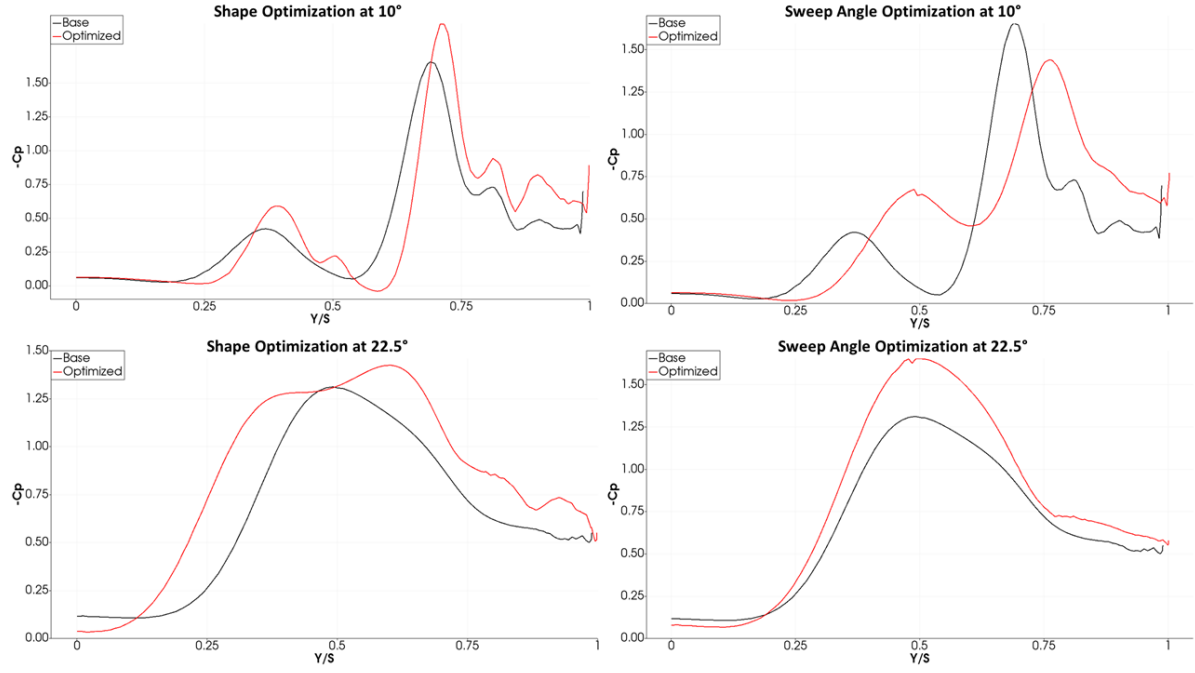


Figure 3.39: Spanwise Pressure Distribution for Baseline and Optimized Designs at 75% of the Chord

angle optimization only at $\alpha = 10^\circ$, the wing vortex suction is reduced, as the strake vortex suction grows significantly. At $\alpha = 22.5^\circ$, the strake and the wing vortices merge and the optimization again enhances the suction induced significantly.

The change in the lift coefficients is given in Table 3.3. As expected the lift coefficients increase significantly for all the optimum configurations. On the other hand, the drag coefficients (Table 3.4) also increase for all cases except the shape optimization case at $\alpha = 10^\circ$. Such increases in drag is attributed to the lift induced drag. But increase in drag is not as much as the increase in the lift. Therefore, the aerodynamic efficiency, C_L/C_D , which is the objective function to be maximized in the optimization is improved in all the cases.

It should be noted that the shape optimizations performed at $\alpha = 10^\circ$ does not improve the aerodynamic efficiency as much as the sweep angle optimization. This is attributed to the main shortcoming of the gradient based optimization process, which can only reach a local maximum.

Table 3.3: Lift Coefficient

Case	Baseline	Optimized	Change
Shape Optimization at $10^\circ\alpha$	0.339	0.349	3.0%
Shape Optimization at $22.5^\circ\alpha$	0.757	0.838	10.8%
Sweep Angle Optimization at $10^\circ\alpha$	0.339	0.387	14.2%
Sweep Angle Optimization at $22.5^\circ\alpha$	0.757	0.832	10.0%

Table 3.4: Drag Coefficient

Case	Baseline	Optimized	Change
Shape Optimization at $10^\circ\alpha$	9.35×10^{-2}	9.23×10^{-2}	-1.3%
Sweep Angle Optimization at $10^\circ\alpha$	9.35×10^{-2}	9.86×10^{-2}	5.5%
Shape Optimization at $22.5^\circ\alpha$	3.63×10^{-1}	3.90×10^{-1}	7.4%
Sweep Angle Optimization at $22.5^\circ\alpha$	3.63×10^{-1}	3.88×10^{-1}	6.9%

Table 3.5: Aerodynamic Efficiency

Case	Baseline	Optimized	Change
Shape Optimization at $10^\circ\alpha$	3.627	3.782	4.3%
Sweep Angle Optimization at $10^\circ\alpha$	3.627	3.926	8.0%
Shape Optimization at $22.5^\circ\alpha$	2.084	2.148	3.1%
Sweep Angle Optimization at $22.5^\circ\alpha$	2.084	2.143	2.8%

CHAPTER 4

CONCLUSIONS

In this thesis, adjoint based optimizations of the strake sweep angle and the leading edge shape are performed by using the open-source CFD toolkit, SU², and DAKOTA to improve the L/D ratio of a strake-wing configuration. SU² flow solutions are first validated on solution adaptive grids against the experimental data. The strake geometry is parametrized using a Free Form Deformation box. The sensitivity of the objective function with respect to the design variable, is obtained with the discrete adjoint solver in SU² suite. The flow and adjoint solutions are performed in a parallel computing environment.

The optimization studies are performed at 0.2 Mach and $Re = 1 \times 10^6$. The leading edge shape optimization study is conducted based on both viscous and inviscid flow solutions at 10° angle of attack. It is shown that although the inviscid optimization process is highly efficient, it does not provide an acceptable optimum solution compared to the one based on the viscous flow solutions.

In the sweep angle optimization, the aerodynamic efficiency is improved by about 8.4% at 10° angle of attack and 2.7% at 22.5° angle of attack. The optimum sweep angles at 10° and 22.5° are found to be 71.6° and 72°. In the leading edge shape optimization, the aerodynamic efficiency is improved by about 4.5% at 10° angle of attack and 3% at 22.5° angle of attack. Yet, the optimum shapes at 10° and 22.5° differ from each other. In all the optimum configurations, the flow solutions show that the wing vortex breakdown is delayed due to the improved interaction with the strake vortex.

The thesis successfully demonstrates that an adjoint based aerodynamic shape opti-

mization process can be employed to a baseline strake-wing configuration to improve its aerodynamic efficiency. The optimization process may further be improved by merging both the shape and the sweep angle optimization processes into one.

REFERENCES

- [1] M. H. Sohn and H. S. Chung, “Effects of strake planform change on vortex flow of a double-delta wing,” *Journal of aircraft*, vol. 44, no. 6, pp. 1842–1848, 2007.
- [2] D. P. Raymer, “Aircraft design: a conceptual approach,” *AIAA Education Series*, 2012.
- [3] J. DEL FRATE and F. ZUNIGA, “In-flight flow field analysis on the nasa f-18 high alpha research vehicle with comparisons to ground facility data,” in *28th Aerospace Sciences Meeting*, p. 231, 1990.
- [4] A. Lippisch, “The development, design and construction of gliders and sailplanes,” *The Aeronautical Journal*, vol. 35, no. 247, pp. 531–578, 1931.
- [5] E. C. Polhamus, *Application of the leading-edge-suction analogy of vortex lift to the drag due to lift of sharp-edge delta wings*. National Aeronautics and Space Administration, 1968.
- [6] E. C. Polhamus, “Predictions of vortex-lift characteristics by a leading-edge suctionanalogy,” *Journal of aircraft*, vol. 8, no. 4, pp. 193–199, 1971.
- [7] E. C. Polhamus, *Charts for predicting the subsonic vortex-lift characteristics of arrow, delta, and diamond wings*. National Aeronautics and Space Administration, 1971.
- [8] J. Smith, “A theory of the separated flow from the curved leading edge of a slender wing,” 1957.
- [9] J. E. Lamar, “Extension of leading-edge-suction analogy to wings with separated flow around the side edges at subsonic speeds,” 1974.
- [10] J. E. Lamar, “Prediction of vortex flow characteristics of wings at subsonic and supersonic speeds,” *Journal of Aircraft*, vol. 13, no. 7, pp. 490–494, 1976.

- [11] C. Rehbach, "Numerical investigation of leading-edge vortex for low-aspect ratio thin wings," *AIAA Journal*, vol. 14, no. 2, pp. 253–255, 1976.
- [12] D. Küchemann, *The aerodynamic design of aircraft*. American Institute of Aeronautics and Astronautics, Inc., 2012.
- [13] J. LAMAR, "Strake-wing analysis and design," in *11th Fluid and PlasmaDynamics Conference*, p. 1201, 1978.
- [14] M. Liu, Z. Lu, C. Qiu, W. Su, X. Gao, X. Deng, and S. Xiong, "Flow patterns and aerodynamic characteristics of a wing-strake configuration," *Journal of Aircraft*, vol. 17, no. 5, pp. 332–338, 1980.
- [15] W. Stuart, *Northrop F-5 Case Study in Aircraft Design*. AIAA professional study series, American Institute of Aeronautics and Astronautics, 1978.
- [16] J. Lamar and J. Campbell, "Recent studies at nasa-langley of vortical flows interacting with neighboring surfaces," 1983.
- [17] J. E. Lamar, "Nonlinear lift control at high speed and high angle of attack using vortex flow technology," *HiR*, 1986.
- [18] H. Chung, C. Seaver, and T. McLaughlin, "Vortex flow control over a delta wing by co-rotating and counter-rotating vortex generator," in *28th AIAA Applied Aerodynamics Conference*, p. 4952, 2010.
- [19] J. M. Luckring, "Aerodynamics of strake-wing interactions," *Journal of Aircraft*, vol. 16, no. 11, pp. 756–762, 1979.
- [20] D. Peake and M. Tobak, "On issues concerning flow separation and vortical flows in three dimensions," *AGARD CP*, no. 342, 1983.
- [21] J. E. Lamar, "Analysis and design of strake-wing configurations," *Journal of Aircraft*, vol. 17, no. 1, pp. 20–27, 1980.
- [22] J. E. Lamar and N. T. Frink, "Aerodynamic features of designed strake-wing configurations," *Journal of Aircraft*, vol. 19, no. 8, pp. 639–646, 1982.
- [23] J. E. Lamar and J. F. Campbell, "Recent studies at nasa-langley of vortical flows interacting with neighboring surfaces," 1983.

- [24] G. E. Erickson and W. P. Gilbert, "Experimental investigation of forebody and wing leading-edge vortex interactions at high angles of attack," 1983.
- [25] D. M. Rao, "Vortical flow management for improved configuration aerodynamics-recent experiences," tech. rep., Vigyan Research Associates Inc. Hampton VA, 1983.
- [26] E. C. Polhamus, "Applying slender wing benefits to military aircraft," *Journal of Aircraft*, vol. 21, no. 8, pp. 545–559, 1984.
- [27] P. J. Bobbitt and J. T. Foughner Jr, "Pivotable strakes for high angle of attack control," *SAE Transactions*, pp. 533–543, 1985.
- [28] D. M. Rao and J. F. Campbell, "Vortical flow management techniques," *Progress in Aerospace Sciences*, vol. 24, no. 3, pp. 173–224, 1987.
- [29] D. Stinton, "Aero-marine design and flying qualities of floatplanes and flying-boats," *The Aeronautical Journal*, vol. 91, no. 903, pp. 97–127, 1987.
- [30] R. Whitford, "Design of a medium military airlifter," in *Aircraft Design and Operations Meeting*, p. 2064, 1989.
- [31] M. Morgan, "A new shape in the sky," *The Aeronautical Journal*, vol. 76, no. 733, pp. 1–18, 1972.
- [32] D. M. Rao, "Vortex control: Further encounters," 1991.
- [33] a. T. Brown, Lee, "Some characteristics and effects of the f/a-18 lex vortices," *AGARD Conference Proceedings 494, Vortex Flow Aerodynamics*, no. 494, 1991.
- [34] M. Bloor and R. Evans, "Strake/delta wing interactions at high angles of attack," 1980.
- [35] C.-H. Hsu, P.-M. Hartwich, and C. Liu, "Computation of vortical interaction for a sharp-edged double-delta wing," *Journal of aircraft*, vol. 25, no. 5, pp. 442–447, 1988.
- [36] K. Fujii and L. B. Schiff, "Numerical simulation of vortical flows over a strake-delta wing," *AIAA journal*, vol. 27, no. 9, pp. 1153–1162, 1989.

- [37] S. G. Reznick and J. Flores, "Strake-generated vortex interactions for a fighter-like configuration," *Journal of Aircraft*, vol. 26, no. 4, pp. 289–294, 1989.
- [38] Y. Xie-yuan, X. Nan, and D. Guo-hua, "Numerical simulation of rolling up of leading/trailing-edge vortex sheets for slender wings," *AIAA journal*, vol. 27, no. 10, pp. 1313–1318, 1989.
- [39] D. Hummel, "On vortex formation over a slender wing at large angles of incidence," in *AGARD CP-247*, 1976.
- [40] S. KERN, "A numerical investigation of vortex flow control through small geometry modifications at the strake/wing junction of a cropped double-delta wing," in *30th Aerospace Sciences Meeting and Exhibit*, p. 411, 1992.
- [41] N. Verhaagen, L. Jenkins, S. Kern, and A. Washburn, "A study of the vortex flow over a 76/40-deg double-delta wing," in *33rd Aerospace Sciences Meeting and Exhibit*, p. 650, 1995.
- [42] J. Ekaterinaris, R. Coutley, L. B. Schiff, and M. Platzer, "Numerical investigation of high incidence flow over a double-delta wing," *Journal of aircraft*, vol. 32, no. 3, pp. 457–463, 1995.
- [43] B. Ashwin Kumar, P. Kumar, S. Das, and J. Prasad, "Effect of leading edge shapes on 81/45 double-delta wing at low speeds," *Proceedings of the Institution of Mechanical Engineers, Part G: Journal of Aerospace Engineering*, vol. 232, no. 16, pp. 3100–3107, 2018.
- [44] T. Arasawa, K. Fujii, and K. Miyaji, "High-order compact difference scheme applied to double-delta wing vortical flows," *Journal of aircraft*, vol. 41, no. 4, pp. 953–957, 2004.
- [45] A. Z. Al-Garni, F. Saeed, and A. M. Al-Garni, "Experimental and numerical investigation of 65 degree delta and 65/40 degree double-delta wings," *Journal of Aircraft*, vol. 45, no. 1, pp. 71–76, 2008.
- [46] X. Zhang, Z. Wang, and I. Gursul, "Interaction of multiple vortices over a double delta wing," *Aerospace Science and Technology*, vol. 48, pp. 291–307, 2016.

- [47] D. Sun, Q. Li, and H. Zhang, “Detached-eddy simulations on massively separated flows over a $76/40^\circ$ double-delta wing,” *Aerospace science and technology*, vol. 30, no. 1, pp. 33–45, 2013.
- [48] Z. Lyu, Z. Xu, and J. Martins, “Benchmarking optimization algorithms for wing aerodynamic design optimization,” in *Proceedings of the 8th International Conference on Computational Fluid Dynamics, Chengdu, Sichuan, China*, vol. 11, 2014.
- [49] J. E. Peter and R. P. Dwight, “Numerical sensitivity analysis for aerodynamic optimization: A survey of approaches,” *Computers & Fluids*, vol. 39, no. 3, pp. 373–391, 2010.
- [50] O. Pironneau, “On optimum profiles in stokes flow,” *Journal of Fluid Mechanics*, vol. 59, no. 1, pp. 117–128, 1973.
- [51] O. Pironneau, “On optimum design in fluid mechanics,” *Journal of Fluid Mechanics*, vol. 64, no. 1, pp. 97–110, 1974.
- [52] A. Jameson, “Aerodynamic design via control theory,” *Journal of scientific computing*, vol. 3, no. 3, pp. 233–260, 1988.
- [53] H. T. Sharp and L. Sirovich, “Constructing a continuous parameter range of computational flows,” *AIAA journal*, vol. 27, no. 10, pp. 1326–1331, 1989.
- [54] D. Bristow and J. D. Hawk, “Subsonic panel method for the efficient analysis of multiple geometry perturbations,” 1982.
- [55] H. ELBANNA and L. CARLSON, “Determination of aerodynamic sensitivity coefficients in the transonic and supersonic regimes,” in *27th Aerospace Sciences Meeting*, p. 532, 1989.
- [56] O. Baysal and M. E. Eleshaky, “Aerodynamic sensitivity analysis methods for the compressible euler equations,” 1991.
- [57] P. D. Frank and G. R. Shubin, “A comparison of optimization-based approaches for a model computational aerodynamics design problem,” *Journal of Computational Physics*, vol. 98, no. 1, pp. 74–89, 1992.

- [58] T. W. Taylor, F. Palacios, K. Duraisamy, and J. J. Alonso, “A hybrid adjoint approach applied to turbulent flow simulations,” in *21st AIAA Computational Fluid Dynamics Conference*, p. 2452, 2013.
- [59] J. C. Newman III, A. C. Taylor III, R. W. Barnwell, P. A. Newman, and G. J.-W. Hou, “Overview of sensitivity analysis and shape optimization for complex aerodynamic configurations,” *Journal of Aircraft*, vol. 36, no. 1, pp. 87–96, 1999.
- [60] W. K. Anderson, J. C. Newman, D. L. Whitfield, and E. J. Nielsen, “Sensitivity analysis for navier-stokes equations on unstructured meshes using complex variables,” *AIAA journal*, vol. 39, no. 1, pp. 56–63, 2001.
- [61] T. W. Sederberg and S. R. Parry, “Free-form deformation of solid geometric models,” in *Proceedings of the 13th annual conference on Computer graphics and interactive techniques*, pp. 151–160, 1986.
- [62] J. A. Samareh, *A novel shape parameterization approach*. NASA Langley Research Center, 1999.
- [63] A. Ronzheimer, “Post-parametrization of cad-geometries using freeform deformation and grid generation techniques,” in *New Results in Numerical and Experimental Fluid Mechanics IV*, pp. 382–389, Springer, 2004.
- [64] J. Brezillon, O. Brodersen, R. Dwight, A. Ronzheimer, and J. Wild, “Development and application of a flexible and efficient environment for aerodynamic shape optimisation,” in *Proceedings of the ONERA-DLR Aerospace Symposium (ODAS), Toulouse, Citeseer*, 2006.
- [65] Z. Lyu, G. K. Kenway, and J. R. Martins, “Aerodynamic shape optimization investigations of the common research model wing benchmark,” *AIAA journal*, vol. 53, no. 4, pp. 968–985, 2015.
- [66] N. R. Secco, J. P. Jasa, G. K. Kenway, and J. R. Martins, “Component-based geometry manipulation for aerodynamic shape optimization with overset meshes,” *AIAA Journal*, vol. 56, no. 9, pp. 3667–3679, 2018.
- [67] K. Leoviriyakit, *Wing planform optimization via an adjoint method*. Stanford University, 2005.

- [68] S. R. Allmaras and F. T. Johnson, “Modifications and clarifications for the implementation of the spalart-allmaras turbulence model,” in *Seventh international conference on computational fluid dynamics (ICCFD7)*, vol. 1902, Big Island, HI, 2012.
- [69] R. Biswas and R. C. Strawn, “Tetrahedral and hexahedral mesh adaptation for cfd problems,” *Applied Numerical Mathematics*, vol. 26, no. 1-2, pp. 135–151, 1998.
- [70] G. Gori, M. Zocca, G. Cammi, A. Spinelli, and A. Guardone, “Experimental assessment of the open-source su2 cfd suite for orc applications,” *Energy Procedia*, vol. 129, pp. 256–263, 2017.
- [71] K. Yutuk, A. Tikenogullari, and I. H. Tuncer, “Numerical investigation of vortical flows over a close-coupled delta canard-wing configuration,” *Computers & Fluids*, vol. 216, p. 104822, 2021.
- [72] B. M. Adams, W. J. Bohnhoff, K. R. Dalbey, J. Eddy, M. Eldred, D. Gay, K. Haskell, P. D. Hough, and L. P. Swiler, “Dakota, a multilevel parallel object-oriented framework for design optimization, parameter estimation, uncertainty quantification, and sensitivity analysis: version 5.0 user’s manual,” *Sandia National Laboratories, Tech. Rep. SAND2010-2183*, 2009.